

University of Dundee

Model studies for flocculation of sand-clay mixtures

Cuthbertson, Alan J. S.; Samsami, Farzin; Dong, Ping

Published in:
Coastal Engineering

DOI:
[10.1016/j.coastaleng.2017.11.006](https://doi.org/10.1016/j.coastaleng.2017.11.006)

Publication date:
2018

Licence:
CC BY-NC-ND

Document Version
Peer reviewed version

[Link to publication in Discovery Research Portal](#)

Citation for published version (APA):

Cuthbertson, A. J. S., Samsami, F., & Dong, P. (2018). Model studies for flocculation of sand-clay mixtures. *Coastal Engineering*, 132, 13-32. <https://doi.org/10.1016/j.coastaleng.2017.11.006>

General rights

Copyright and moral rights for the publications made accessible in Discovery Research Portal are retained by the authors and/or other copyright owners and it is a condition of accessing publications that users recognise and abide by the legal requirements associated with these rights.

Take down policy

If you believe that this document breaches copyright please contact us providing details, and we will remove access to the work immediately and investigate your claim.

Model Studies for Flocculation of Sand-Clay Mixtures

Alan J.S. Cuthbertson^{1,*}, Farzin Samsami² and Ping Dong³

¹ Associate Professor in Sediment Processes, School of Energy, Geoscience, Infrastructure and Society,
Heriot-Watt University, Edinburgh EH14 4AS, UK.

² Postdoctoral Research Associate, School of Energy, Geoscience, Infrastructure and Society, Heriot-Watt
University, Edinburgh EH14 4AS, UK.

³ Professor of Civil Engineering, School of Engineering, University of Liverpool, Liverpool L69 EBX, UK.

* Corresponding author, a.cuthbertson@hw.ac.uk

ABSTRACT

Results are presented from a combined experimental and numerical study aimed at comparing the flocculation behaviour of purely-cohesive (clay) and mixed (sand-clay) sediment suspensions under equivalent controlled hydrodynamic conditions. The experiments were conducted in a grid-stirred settling column and focussed on measuring the parametric influences of grid-generated shear rate and local suspended sediment concentrations on the time-evolution of the micro- and macrofloc size distributions generated in the column, as well as representative maximal and root-mean-square floc sizes. The results indicate that for kaolin clay suspensions under low-medium shear rates, initial aggregation rates and the peak or quasi-equilibrium floc sizes attained increase with the clay input concentration; this latter effect due to the larger proportion of macroflocs generated within these runs. By contrast, under high shear rates, representative floc sizes for kaolin clay suspensions remain largely unchanged over the experimental duration, with little influence from clay input or in-situ concentrations, and no macroflocs present in the resulting floc size distributions. The addition of the fine sand fraction to the kaolin clay suspensions is shown to reduce both initial aggregation rates and the representative floc sizes attained in the column for runs under low-medium shear rates, whilst having negligible effect on the flocculation behaviour for the sand-clay mixtures under high shear rates. These results suggest that the sand fraction inhibits flocculation at lower shear rates due to an additional floc break-up mechanism resulting from direct sand-clay interactions (e.g. particle-floc collisions). The importance of these inter-fractional (sand-clay) interactions diminishes, in comparison to shear-induced floc break-up, under higher shear conditions. A one dimensional vertical (1DV) model incorporating a population balance equation (PBE) that includes new representation of these multi-fractional (sand-clay) collisions is applied to simulate the kaolin clay and sand-clay settling column tests. In general, the 1DV PBE model predictions provide good agreement with the measured in-situ concentrations and quasi-equilibrium floc sizes attained, but under-predict floc sizes during the initial aggregation phase due to uncertainty with the upper boundary condition in the 1DV model domain. Furthermore, the reliance of the 1DV PBE model predictions on empirical floc break-up rates associated with shear-induced floc fragmentation and multi-fractional (sand-clay) collisions warrants further attention to better define the microscale dynamics of these processes for their improved representation in the PBE model. It is anticipated that this multi-fractional approach represents an improved basis for modelling flocculation processes within natural sedimentary environments, such as estuaries and tidal inlets, where bed sediments often consist of interacting cohesive (i.e. muds) and non-cohesive (i.e. silts, sands) fractions.

Keywords: Flocculation; mixed sediments; sand-clay mixtures; settling column; grid-generated shear; 1DV model; population balance equation.

1. Introduction

Natural sedimentary environments such as estuaries are amongst the most dynamic of coastal zones due to strong variability in sediment fluxes generated by natural hydrodynamic forcing from tidal currents and/or waves, as well as anthropogenic interventions such as dredging operations, port and harbor developments, coastal structures and energy installations. Subtidal and intertidal sediments within these environments typically consist of cohesive muds (e.g. clays and organic matter) and non-cohesive fractions (e.g. fine sands and silts), which can vary significantly in proportion both spatially and temporally [1]. The nature of interactions that exist between cohesive and non-cohesive sediments has important implications for modelling transport processes such as flocculation, settling, deposition, erosion and consolidation [2–4] and, ultimately, morphodynamic evolution within estuaries. While the physical behavior of mixed (sand-mud) sediments is known to be significantly different from that of the individual fractions [5], many previous studies [6–12] have considered estuaries and tidal inlets as predominantly segregational environments, where the mud and sand fractions are treated largely as independent, non-interacting regimes. As such, there is an acknowledged lack of quantitative information on the key parametric influences on sand-mud interactions in suspension, and their effects on flocculation and settling within mixed sedimentary systems [13].

For purely cohesive sediments, flocculation (i.e. particle aggregation and break-up) is known to result from inter-particle collisions due to Brownian motion, turbulent mixing and differential settling [14–16]. Many flocculation models for cohesive suspensions are based on the hierarchical “order of aggregation” approach [17], whereby primary mud particles agglomerate to form small, dense microflocs (i.e. $D_f \leq \sim 150 \mu\text{m}$), which in turn can flocculate to form larger, more fragile, macroflocs ($D_f \geq \sim 150 \mu\text{m}$) [18,19]. It is generally accepted that for a given primary particle concentration, aggregation rates and, hence, floc sizes will tend to increase with the turbulence intensity due to an increased number of inter-particle collisions. However, the same turbulent motions also generate shear stresses that can limit floc growth due to disruption and break-up of macroflocs [16,20]. Most previous laboratory and in-situ field investigations have shown a strong inverse relationship exists between measured floc sizes and turbulent shear rates [3,14,20–26]; only at very low shear rates (i.e. $G < 35 \text{ s}^{-1}$ [27]), where aggregation dominates over break-up processes, has floc growth been observed with increasing turbulent shear rates.

Previous flocculation research also indicates that the influence of particle concentration is not as straightforward as conventional wisdom or common assumptions on aggregation behaviour may suggest (i.e. higher concentrations \rightarrow increased inter-particle collisions \rightarrow higher aggregation rates and increased floc sizes) [28]. While some experimental studies [29,30] support this hypothesis, other investigations [3,20,31] found limited or no systematic correlation

between floc sizes generated and mass concentration. Indeed, the study by Tsai et al. [32] indicated the opposite trend, with reduced floc sizes attained at higher particle mass concentrations, leading Lick and Lick [33] to suggest that, under specific parametric conditions, inter-floc collisions may be more important in the break-up process than fluid shearing. The temporal variability in these aggregation and break-up processes also results in continually-evolving floc properties (e.g. floc size and density), non-equilibrium suspended sediment loads and settling fluxes [3,24,34]. Cuthbertson et al. [3] conducted grid-stirred settling column experiments to investigate the temporal evolution of kaolin clay flocs forming under a range of turbulent shear rates and “single-shot” particle mass concentrations. They found that the highest initial aggregation rates and largest (macro-) flocs were generated under low turbulent shear conditions, with lower aggregation rates and smaller (micro-) flocs generated under higher turbulent shear conditions. However, for the time-varying conditions generated by the “single-shot” clay input, the observed flocculation behavior was largely controlled by resulting concentration gradients in the column that influenced both the floc settling rates and flocculation time scales (i.e. time to attain the so-called *equilibrium* floc size, where aggregation and break-up processes balance [35]).

In comparison to these extensive studies on purely cohesive (mud) flocculation, there remain significant knowledge gaps in the physical understanding of flocculation and settling behaviour for sand-mud mixtures. Recent experimental studies [36,37] found that the contributions to the mass settling flux from microflocs (i.e. $D_f \leq 160 \mu\text{m}$) and macroflocs (i.e. $D_f \geq 160 \mu\text{m}$) tend to increase and reduce, respectively, with increasing sand content, leading to the hypothesis that the sand grains tend to interact more with the smaller, denser microfloc structures than with the larger, more fragile macroflocs. By contrast, Cuthbertson et al. [3] demonstrated that the aggregation rates and floc sizes generated in pure kaolin clay suspensions under non-equilibrium conditions were inhibited significantly by the addition of sand. It is suggested that this demonstrates the role of (i) direct collisions between sand particles and clay macroflocs, and/or (ii) indirect particle-fluid interactions and self-induced turbulence within mixed (sand-clay) suspensions, in increasing the break-up rate of macroflocs, and thus inhibiting their formation in the mixed (sand-clay) suspensions. However, as there have been relatively few systematic experimental studies aimed at determining the parametric influences on the flocculation of sand-mud mixtures, the influence of inter-fractional interactions on aggregation and break-up processes remains largely ignored in flocculation modelling studies.

The main aim of the current study is therefore to investigate experimentally the parametric controls on the flocculation behaviour of both purely cohesive (kaolin clay) and mixed (sand-clay) suspensions for prescribed sediment feed conditions and controlled hydrodynamic forcing generated in a grid-stirred settling column. Specifically, the clay and sand fractions are added (where applicable) continuously over a specified feed duration, with the resulting temporally-increasing mass concentrations in the settling column designed to replicate, to some extent, the increases in suspended

concentrations that typically occur during the build up to an estuarine turbidity maximum [38]. The study extends on from the previous experimental work by Cuthbertson et al. [3] by measuring the temporal evolution of representative floc sizes (i.e. maximal $D_{f,95}$; $D_{f,90}$ and root-mean-square $D_{f,rms}$) both during the initial aggregation phase (i.e. $dD_f/dt > 0$, under *non-equilibrium* conditions) and the transition to *quasi-equilibrium* flocculation conditions (i.e. $dD_f/dt \approx 0$) within the settling column. Here, the kaolin-only runs are therefore used to provide base-line data against which the parametric influences of the sand fraction in the sand-clay mixture runs could be assessed quantitatively.

The second aim of the study is to simulate these kaolin-only and sand-clay settling column runs through the application of a one-dimensional vertical (1DV) advection-diffusion model coupled to a multi-fractional population balance equation (PBE) approach. A key new aspect of this numerical study is the inclusion in the PBE of additional floc break-up terms to account for the effects of sand particle – clay floc collisions, and determine their influence on floc growth rates and maximum floc sizes attained in the sand-clay mixture runs. To the best of the authors' knowledge, this is the first time that inter-fractional (sand-clay) break-up terms have been included in a 1DV PBE model approach. As such, the experimental datasets from the kaolin-only and sand-clay settling column runs are used to verify the aggregation and break-up terms specified in this new, multi-fractional PBE model, thus enabling the quantitative contributions associated with floc growth (i.e. floc-floc collisions) and break-up (i.e. floc breakage; sand particle – clay floc collisions) to be isolated within the model simulations.

2. Experimental Set-up and Methodology

2.1 Settling Column Arrangement

Figs. 1(a) and (b) show a schematic representation of the settling column used in the experimental studies and a labelled image of the system in operation, respectively. The column arrangement consists of a 50 litre capacity upper buffer mixing tank; a 2.1 m-long main column section, constructed from circular acrylic pipe with an internal diameter of 0.24 m (5 mm wall thickness); and an *in-situ* floc measurement section at the bottom of the column. For the experimental runs, the column and buffer tank were filled with clear, fresh water ($\rho_w = 1000 \text{ kg.m}^{-3}$).

A rigid array of eight interconnected grids, each horizontally-orientated and vertically aligned at a fixed spacing $H = 200 \text{ mm}$ is used to generate controlled hydrodynamic forcing conditions within the main column section. These grids are connected to an external drive mechanism, allowing them to oscillate with a predefined stroke (i.e. $S = 53 \text{ mm}$) and frequency (i.e. $f = 0.2 - 0.6 \text{ s}^{-1}$). Each grid has a uniform square mesh pattern of “hole” size $M = 45 \text{ mm}$ and “bar”

thickness $m = 9$ mm, with the resulting ratio $M/m = 5$ and corresponding grid solidity of 29% in accord with the geometrical configuration adopted previously for grid turbulence studies [39,40].

2.2 Sediment Input Conditions

Prior to each experimental run, concentrated water-clay suspensions with mass concentration $C_m = 1.2, 1.8$ and 2.4 g.l^{-1} were prepared within an external mixing tank by adding measured quantities (60, 90 and 120 g) of kaolin clay [*Polwhite B*; $d_{25}: d_{50}: d_{90} = 0.6: 2.0: 8.5 \text{ }\mu\text{m}$; plastic (PL) and liquid (LL) limits = 28% and 54%, respectively; specific gravity $\gamma_m = 2.59$] to a set volume (50 l) of fresh water. These suspensions were mixed vigorously prior to and during the experimental run with submersible pumps to ensure that the input concentration remained uniform throughout the test and the kaolin clay particles remained in a largely unflocculated state. The concentrated kaolin-water mixture was fed into the buffer tank via a peristaltic pump set at a constant feed rate of 0.3 l.min^{-1} (i.e. 0.005 l.s^{-1}), where it was further mixed and diluted by rotating paddles [Figs. 1(a) and (b)]. The counter-rotation of the two mixing paddles generated an established circulation in the buffer tank leading to the gradual transfer of the dilute clay suspension into the main column section, where it was subjected to the prescribed turbulent flow conditions generated by the oscillating grids. In general, the duration of kaolin feed into the buffer tank lasted between 140 and 215 minutes, with the experimental floc measurements continuing after the clay-water feed was stopped (for a total run duration of up to 6 hours). The main experimental variables within each of the individual runs performed in the study are presented in Table 1.

For experimental runs considering the flocculation characteristics of sand-clay mixtures, the kaolin suspension was prepared and fed into the buffer tank, as described above. The non-cohesive fraction was an extra fine sand [*CLS33-Superfine high silica sand*; $D_s = 75 - 500 \text{ }\mu\text{m}$; $D_{s,50} = 150 \text{ }\mu\text{m}$; specific gravity $\gamma_s = 2.64$], which was added directly into the main column section as a continuous, dry feed via a calibrated vibration feeder, sited above the buffer tank [Fig. 1(b)]. The sand feed rate I_R was varied between $1.99 - 4.70 \text{ g.min}^{-1}$ and continued throughout the full duration of each run. This direct, continuous, dry sand feed method was adopted to prevent mass sand deposition within the upper buffer tank and due to the expectation that the column residence time of the sand particles would be 1-2 orders of magnitude shorter than the kaolin flocs forming within the column (based on predicted settling velocities).

2.3 Concentration Measurement and Floc Characterisation

Total suspended sediment (TSS) concentrations were measured as a continuous time-series record at two locations in the main column section using optical backscatter (OBS) probes [i.e. at the mid-elevation within the oscillating grid array (OBS₁) and directly beneath the array (OBS₂), Fig. 1(a)]. These OBS probes were calibrated over a wide range of

sand-clay mixtures (sand: $C_s = 0 \rightarrow 5 \text{ g l}^{-1}$; clay: $C_c = 0 \rightarrow 1 \text{ g l}^{-1}$), with relationships established between the turbidity (NTU) and total suspended sediment concentrations (i.e. $\text{TSS} = C_c + C_s$) at both measurement locations.

An *in-situ* floc measurement section [Fig. 1(a)] was designed to permit recording and analysis of the flocs generated within the main column section under the influence of the oscillating grid turbulence. This measurement section was installed directly below the main, grid-stirred, column section and was designed to sample small (but statistically-significant) volumes of the flocs, through the opening and closing of a narrow slotted gate, at specific elapsed times throughout each individual run. These floc samples entering the viewing chamber were illuminated by a vertically-orientated YAG pulsed laser light sheet and recorded (at 30 frames per second) using a Point Grey Grasshopper digital CCD Camera with a 3.3X macro lens that permitted a maximum image resolution of 1932×1452 pixels [i.e. 1 pixel = $3.78 \text{ } \mu\text{m}$, see Fig. 2(a)]. The image analysis software package ImageJ [41] was used to identify the individual flocs and their geometrical properties (e.g. surface area, perimeter, circularity, etc.) [Fig. 2(b) and (c)] through application of appropriate image filtering (for noise removal) and intensity thresholds to the raw floc images.

A nominal equivalent floc diameter D_f was calculated for each identified floc from their measured surface area A_f , such that $D_f = 2(A_f/\pi)^{1/2}$ [42]. Similarly, nominal equivalent floc volumes $V_f = (4/3)\pi D_f^3$ were also calculated to plot floc size distribution curves in terms of floc volumetric fractions. To enable quantitative analysis of the temporal variations in floc size characteristics throughout each experimental run, the root-mean-square $D_{f,rms}$ and maximal $D_{f,95}$ (and $D_{f,90}$) floc sizes were determined, such that:

$$D_{f,rms} = \sqrt{\frac{1}{n} \sum_{i=1}^n D_{f,i}^2} \quad (1)$$

where n is the total number of flocs identified at a given sample period. The maximal floc sizes $D_{f,95}$ (and $D_{f,90}$) were obtained from the calculated ensemble average of the largest 5% (and 10%) of these identified flocs. Validation of flocs included in this ensemble-averaging procedure was conducted to ensure that each floc was singular (i.e. non-overlapping) and fully focused within the laser light sheet. For runs with sand-clay mixtures, illuminated sand particles were also discounted from the floc averaging procedure. It is noted here that the floc images could not be used to define explicitly the respective roles of aggregation processes (i.e. due to clay floc–floc collisions) and break-up processes (i.e. due to shear-induced floc breakage or sand particle – floc collisions) in floc development as the microscale dynamics of these interactions could not be measured directly within the settling column.

2.4 Grid Turbulence Characteristics

The oscillating grid arrangement within the settling column was shown in [3] to generate controlled hydrodynamic forcing conditions consisting of near-isotropic, zero-mean-shear turbulence in the central flow region between the grids. Based on the analysis of turbulence characteristics generated by the oscillating grid array, the vertical distribution of root-mean-square turbulence intensities $u'_{rms}(z)$ and $v'_{rms}(z)$ between individual grid pairs can be defined non-dimensionally, based on grid characteristics [3] as

$$\frac{u'_{rms}(z)}{f.H}, \frac{v'_{rms}(z)}{f.H} = C_g M^{1/2} S^{3/2} \left[\left(\frac{H}{2} \right)^2 - z^2 \right]^{-1/2}, \quad (2)$$

where C_g is an empirically-derived coefficient [3], M is the grid mesh “hole” size, S is the oscillation stroke, z is the vertical displacement from the mid-elevation (i.e. $z = 0$) between the grids, f is the oscillation frequency and H is the grid spacing. Within the current experiments, the mesh size grid M , oscillation stroke S and grid spacing H were fixed at 0.045, 0.05 and 0.2 m, respectively. With the assumption that the grid-generated turbulence is approximately isotropic, the turbulent kinetic energy k and dissipation ε for the grid-generated turbulence can be estimated following the procedure outlined in [3]. The turbulent shear rate (or dissipation parameter) G is an important parameter controlling the flocculation (aggregation) and break-up (disaggregation) of mud flocs [16] and can be estimated directly from the formulation proposed by Camp and Stein [43]

$$G = \sqrt{\frac{\varepsilon}{\nu}} \approx \sqrt{\frac{u'^3_{rms}}{l_x \nu}}, \quad (3)$$

where l_x is the integral length scale of the grid turbulence and ν is the kinematic viscosity. Estimated values for the minimum and maximum turbulent shear rate G are presented in Table 1 for a given oscillating grid frequency f (i.e. $f = 0.2, 0.4$ and 0.6 s^{-1}), utilising UVP-measured u'_{rms} turbulence intensities and estimated integral length scales l_x at the mid-elevation between grid pairs (i.e. $z/H = 0$) and in close vicinity of the oscillating grids (i.e. $z/H \rightarrow \pm 0.475$), respectively. It is noted from Table 1 that the estimated G values increase by about 2 orders of magnitude between the quasi-isotropic turbulence region at the mid-elevation and the flow region adjacent to the grids. The estimated G values are also shown to vary by a factor of ~ 5 over the three grid oscillation frequencies tested.

3. Experimental Results

3.1 Concentration Distribution in Settling Column

Fig. 3 shows example time series plots of turbidity (NTU) measured by the OBS probes at the mid-height (OBS₁) and bottom (OBS₂) of the oscillating grid array, with moving average trend lines (i.e. over 11 minutes or 61 data measurements) indicating the general temporal variation in turbidity at the two column locations during the

experimental runs. Fig. 3(a) and (b) show directly comparable datasets for kaolin clay and sand-clay mixture suspensions (i.e. TN3 and TNS3, respectively, see Table 1) for otherwise identical oscillating grid and clay feed conditions. It is noted here that, under the lowest grid shear conditions tested (i.e. $G = 0.73 - 46.6 \text{ s}^{-1}$, Table 1), OBS_1 and OBS_2 turbidity values increase monotonically over the full run duration, indicating that equilibrium concentrations are not attained in the column. Comparing Figs. 3(a) and (b) directly, the turbidity values for the sand-clay run [TNS3, Fig. 3(b)] are significantly lower than in the kaolin clay run [TN3, Fig. 3(a)]. This is somewhat unexpected as the OBS calibration measurements indicated that the addition of fine sand (i.e. $C_s = 0 \rightarrow 5.0 \text{ g l}^{-1}$) would increase the measured NTU values, compared to equivalent kaolin clay suspensions ($C_c = 0 \rightarrow 1.0 \text{ g l}^{-1}$). This suggests that the presence of the fine sand fraction must inhibit the downward motion of the clay suspension in the settling column due to either (i) reduced flocculation rates (and, hence, floc settling rates) under weak, grid-generated turbulence, or (ii) differential settling and wake effects induced by the rapidly settling sand particles. Indeed, turbidity (NTU) measurements for a sand-clay suspension with higher sand content (i.e. TNS4, Table 1) are shown to reduce further compared to the equivalent kaolin clay suspension, under otherwise identical conditions.

Similarly, direct comparison of Figs. 3(c) and (d) for kaolin clay and sand-clay mixture suspensions generated under higher shear rate conditions (i.e. $G = 2.07 - 123.5 \text{ s}^{-1}$; TN5 and TNS1, respectively) also indicate a reduction in NTU values when the sand fraction is present within the column. In both cases here, the moving-average trend line for OBS_1 measurements approaches an equilibrium NTU value (~ 320 and ~ 300 , respectively) after an elapsed time of ~ 175 mins, while the temporal lag in OBS_2 measurements results in similar equilibrium NTU values being approached near the end of the runs (i.e. $t \rightarrow 350$ mins.). Finally, under the highest shear conditions tested (i.e. $G = 3.79 - 226.8 \text{ s}^{-1}$), direct comparison between NTU values for the kaolin clay [Fig. 3(e)] and sand-clay mixture [Fig. 3(f)] suspensions indicate similar overall temporal variations, with a comparable time lags between OBS_1 and OBS_2 measurements (i.e. equilibrium NTU values of ~ 320 and ~ 290 attained at $t = \sim 165$ mins and ~ 225 mins, respectively). It is also noted that the initial rate of turbidity increase at OBS_1 and OBS_2 is larger for runs at higher shear rates, indicating that turbulent diffusion in the grid-stirred column increases with shear rate G , as expected. In the remainder of the paper, OBS_1 and OBS_2 measurements are presented as total suspended sediment (TSS) concentrations following calibration.

3.2 Flocculation for Kaolin Clay Suspensions

Fig. 4 presents size distributions for kaolin clay flocs recorded in the floc viewing chamber [Fig. 1(a)] for clay-only suspensions. These floc size distribution (FSD) plots are derived from calculated volumetric fractions for individual floc size classes i , each with representative mean floc diameters D_{fi} . Floc size distributions obtained for the lowest grid shear

and clay input concentration conditions [i.e. TN1: $G = 0.73 - 43.6 \text{ s}^{-1}$; $C_m = 1.2 \text{ g l}^{-1}$, Fig. 4(a)] have typically high volumetric proportions (between ~25% and ~34%) of smaller microflocs ($D_f < 63 \text{ }\mu\text{m}$), with the proportion of macroflocs ($D_f > 150 \text{ }\mu\text{m}$) generally lower, but increasing (i.e. 0% \rightarrow ~13%) over the experiment duration. At higher clay input concentrations [i.e. TN3: $C_m = 1.8 \text{ g l}^{-1}$, Fig. 4(b)], the proportion of smaller microflocs is significantly lower and reduces (i.e. 21% \rightarrow 11%) over the experiment duration, while the proportion of macroflocs increases (up to ~45%) over the run duration. For the medium grid shear condition (i.e. $G = 2.07 - 123.5 \text{ s}^{-1}$), floc size distributions at the lower clay input condition [i.e. TN4: $C_m = 1.2 \text{ g l}^{-1}$, Fig. 4(c)] again have larger volumetric proportions of smaller microflocs (between ~17% and ~30%) compared to macroflocs (up to ~14%), but with no obvious increasing or decreasing trends over the experiment duration. At higher clay input concentrations [i.e. TN5: $C_m = 1.8 \text{ g l}^{-1}$, Fig. 4(d)], notable reductions and increases, respectively, in the smaller microfloc (between ~13% and ~24%) and macrofloc (between ~10% and ~38%) populations are again observed. Finally, for runs at the highest grid shear condition ($G = 3.79 - 226.8 \text{ s}^{-1}$) [i.e. TN7 and TN8: $C_m = 1.2 \text{ g l}^{-1}$ and 1.8 g l^{-1} , Figs. 4(e) and (f)], while no macroflocs are generated, smaller microfloc fractions vary typically between ~25% and ~46% during the runs. In summary, the measured floc size distributions generally indicate that an increase in the input clay concentration C_m leads to a reduction in the abundance of smaller microflocs ($D_f < 63 \text{ }\mu\text{m}$) and a corresponding increase in the macrofloc ($D_f > 150 \text{ }\mu\text{m}$) populations. The results also demonstrate a general trend of increasing microfloc ($D_f < 63 \text{ }\mu\text{m}$) and reducing macrofloc ($D_f > 150 \text{ }\mu\text{m}$) populations with increasing shear rate G conditions in the settling column. These findings are in general accord with the expected parametric influences of clay input concentration C_m and shear rate G on the floc sizes generated in the grid-stirred settling column [3], which will be discussed in detail later.

To better understand the temporal variations in the floc size distributions generated for kaolin clay suspensions, representative maximal $D_{f,95}$, $D_{f,90}$ and root-mean-square $D_{f,rms}$ floc sizes are calculated. Fig. 5 shows the time series of these representative floc sizes in the kaolin clay runs with the same parametric combinations of clay input concentration C_m and grid-generated shear G conditions, as shown in Fig. 4. These plots also present corresponding time series measurements of total suspended sediment (TSS) concentrations at the OBS₁ and OBS₂ positions in the column (Fig. 1). At the lowest shear and clay input conditions [i.e. TN1: $G = 0.73 - 43.6 \text{ s}^{-1}$; $C_m = 1.2 \text{ g l}^{-1}$, Fig. 5(a)], the initial floc growth is highlighted by the temporal increase in maximal $D_{f,95}$ floc sizes (i.e. $106 \text{ }\mu\text{m} \rightarrow 139 \text{ }\mu\text{m}$ for $t = 96 \rightarrow 211$ mins). This initial aggregation rate $dD_{f,95}/dt = 0.30 \text{ }\mu\text{m}/\text{min}$ [i.e. gradient of best-fit trend line in Fig. 5(a)] is shown to reduce significantly at later elapsed times [i.e. $dD_{f,95}/dt = 0.07 \text{ }\mu\text{m}/\text{min}$, Fig. 5(a)], with the peak maximal floc size $D_{f,95} = 148 \text{ }\mu\text{m}$ attained at $t = 344$ mins. These general trends are mirrored by the temporal variation of the $D_{f,90}$ floc sizes, while the $D_{f,rms}$ floc sizes remain relatively consistent throughout the run [i.e. $D_{f,rms} = 68 - 75 \text{ }\mu\text{m}$, Fig. 5(a)]. This is

consistent with the relative invariability in smaller microflocs ($D_f < 63 \mu\text{m}$), and the significant increase in macroflocs ($D_f > 150 \mu\text{m}$), observed in the corresponding FSDs [Fig. 4(a)] over the run duration. The temporal increase in $D_{f,95}$ values also coincides with the monotonic increase in TSS clay concentrations measured at OBS₁ and OBS₂ positions, indicating the significant parametric role that concentration plays in the initial aggregation processes. Fig. 5(b) shows that a higher initial aggregation rate (i.e. $dD_{f,95}/dt = 0.53 \mu\text{m}/\text{min}$) occurs at the higher clay input condition [i.e. run TN3: $C_m = 1.8 \text{ g l}^{-1}$, Table 1], reaching a peak maximal floc size $D_{f,95} = 187 \mu\text{m}$ at $t = 225 \text{ min}$, before reducing slightly (i.e. $D_{f,95} \rightarrow 176 \mu\text{m}$) over the remainder of the run. Corresponding $D_{f,90}$ and $D_{f,rms}$ floc sizes also show an initial aggregation phase up to their maximum values (i.e. $D_{f,90} = 176 \mu\text{m}$; $D_{f,rms} = 95 \mu\text{m}$ at $t = 225 \text{ mins}$), followed by a slight reduction over the remainder of the run. This is again in general accord with the observed temporal changes in smaller microfloc ($D_f < 63 \mu\text{m}$) and macrofloc ($D_f > 150 \mu\text{m}$) populations in the FSDs [Fig. 4(b)]. In particular, these results suggest that, while TSS concentrations in the column increase throughout the experiment duration, $D_{f,95}$, $D_{f,90}$ and $D_{f,rms}$ floc sizes can attain peak or *quasi-equilibrium* values during the run, with the slight reductions in floc sizes in later stages potentially related to the finite duration of the kaolin clay feed (see Table 1).

For the medium shear condition (i.e. $G = 2.07 - 123.5 \text{ s}^{-1}$), a larger initial aggregation rate (i.e. $D_{f,95}/dt = 0.66 \mu\text{m}/\text{min}$) is again obtained for the higher clay input run [i.e. TN5: $C_m = 1.8 \text{ g l}^{-1}$, Fig. 5(d)], compared to the lower clay input condition [i.e. TN4: $C_m = 1.2 \text{ g l}^{-1}$, Fig. 5(c)], where $D_{f,95}/dt = 0.37 \mu\text{m}/\text{min}$. This is consistent with the initial growth rates observed for the $D_{f,90}$ and $D_{f,rms}$ floc sizes for both clay input conditions. Subsequent to this initial aggregation phase, these representative floc sizes for both runs [Fig. 5(c) and (d)] again reduce slightly from their peak values attained during the runs. It is also noted that the measured OBS₁ and OBS₂ concentrations tend to the same equilibrium levels within the column [i.e. TSS $\rightarrow \sim 0.6 \text{ g l}^{-1}$, Fig. 5(c); TSS $\rightarrow \sim 0.95 \text{ g l}^{-1}$, Fig. 5(d)], but at different elapsed times, with a notable temporal lag between the two measurements positions. In both cases, the representative floc sizes reach their peak or *quasi-equilibrium* values before equilibrium concentrations are attained at both OBS₁ and OBS₂ positions in the column. This may again be associated with the finite-duration feed times of kaolin clay into the column (i.e. $t_m = 152$ and 170 mins , Table 1). However, Figs. 5(c) and (d) [and corresponding FSDs in Figs. 4(c) and (d)] indicate that larger equilibrium concentrations [i.e. TSS $\rightarrow 0.95 \text{ g l}^{-1}$, Fig. 5(d)] also correspond to larger macroflocs ($D_f > 150 \mu\text{m}$) populations and maximal floc sizes ($D_{f,95}$ and $D_{f,90}$) being generated in the settling column, in general accord with aggregation theory [17].

For the highest shear rate condition (i.e. $G = 3.79 - 226.8 \text{ s}^{-1}$), Figs. 5(e) and (f) indicate minimal temporal variation in the measured $D_{f,95}$, $D_{f,90}$ and $D_{f,rms}$ floc sizes over the full experiment duration, with no indication of the initial

aggregation phase in either run (i.e. $dD_{f,95}/dt \approx 0$). This suggests that aggregation and break-up are approximately balanced from an early stage within these runs. Comparing Figs. 5(e) and (f) directly, there is a slight increase in representative floc sizes for the larger clay input concentration [i.e. TN8: $C_m = 1.8 \text{ g l}^{-1}$, Fig. 5(f)], compared to the lower input condition [i.e. TN7: $C_m = 1.2 \text{ g l}^{-1}$, Fig. 5(e)], but no discernible influence on these floc sizes from the temporal variation in concentrations within the column. As such, it is anticipated that high shear rates dominate the aggregation and break-up behaviour in the kaolin clay suspensions, as evidenced by the preclusion of macroflocs ($D_f > 150 \text{ }\mu\text{m}$) under these conditions [see FSDs in Figs. 4(e) and (f)].

3.4 Flocculation for Sand-Clay Mixture Suspensions

Fig. 6 presents similar temporal variations in the representative maximal $D_{f,95}$, $D_{f,90}$ and root-mean-square $D_{f,rms}$ floc sizes and corresponding TSS concentration measurements for the sand-clay mixtures tested in runs TNS1 – TNS6 (see Table 1). Figs. 6(a) and (b) show plots for runs conducted under the lowest shear condition (i.e. TNS3 and TNS4: $G = 0.73 - 43.6 \text{ s}^{-1}$), with the same kaolin clay input condition (i.e. $C_m = 1.8 \text{ g l}^{-1}$), but different sand input rates ($I_s = 2.0 \text{ g min}^{-1}$ and 4.15 g min^{-1} , respectively). For the lower sand input [i.e. Fig. 6(a)], the initial aggregation rate (i.e. $dD_{f,95}/dt = 0.50 \text{ }\mu\text{m/min}$) is slightly lower than for the equivalent kaolin clay run [i.e. TN3: $dD_{f,95}/dt = 0.53 \text{ }\mu\text{m/min}$, Fig. 5(b)], while the higher sand input [Fig. 6(b)] reduces this initial aggregation rate significantly (i.e. $dD_{f,95}/dt = 0.14 \text{ }\mu\text{m/min}$). The influence of the sand fraction is also shown to reduce the peak $D_{f,95}$, $D_{f,90}$ and $D_{f,rms}$ floc sizes attained in the column when compared to corresponding values for the kaolin clay suspension [i.e. TN3, Fig. 5(b)]. Here, it is apparent that macroflocs ($D_f > 150 \text{ }\mu\text{m}$) are almost completely absent from the two sand-clay mixtures shown in Figs. 6(a) and (b). Furthermore, the concentration time series at both OBS₁ and OBS₂ positions are significantly reduced for the two sand-clay mixtures [Figs. 6(a) and (b)], when compared to the equivalent kaolin clay suspension [Fig. 5(b)]. This effect may be indicative of (i) the increased presence of smaller microflocs with reduced settling rates, and/or (ii) increasingly hindered settling of these microflocs due to upward fluid displacement by the faster settling sand particles [2].

Under the medium shear condition ($G = 2.07 - 123.5 \text{ s}^{-1}$), two sand-clay mixture runs (i.e. TNS1 and TNS5, Table 1) were conducted for different sand input rates (i.e. $I_s = 2.26 \text{ g min}^{-1}$ and 3.90 g min^{-1} , respectively). Figs. 6(c) and (d) again indicate that both the initial aggregation rates and peak maximal $D_{f,95}$ floc sizes attained for these sand-clay mixtures are significantly lower than for the equivalent kaolin clay suspension [i.e. TN5, Fig. 5(d)]. This suggests that the presence of the sand fraction hinders both the initial clay floc development and the maximum sizes that can be generated in the settling column for given shear rates and kaolin clay input conditions. Comparing Figs. 6(c) and (d), however, the significant differences in the representative floc sizes obtained for sand feed rates $I_s = 2.26 \text{ g min}^{-1}$ [Fig.

6(c)] and 3.90 g min^{-1} [Fig. 6(d)] are somewhat unexpected as the larger sand input would be expected to inhibit floc development (and, hence, floc sizes and settling rates) to a greater extent in the column. Finally, at the highest grid shear condition ($G = 3.79 - 226.8 \text{ s}^{-1}$), two sand-clay mixture runs (i.e. TNS2 and TNS6, Table 1) with different sand input rates (i.e. $I_s = 1.99$ and 4.70 g min^{-1} , respectively) are shown in Figs. 6(e) and (f), respectively. Here, the maximal $D_{f,95}$, $D_{f,90}$ and root-mean-square $D_{f,rms}$ floc sizes are largely similar to those obtained for the equivalent kaolin clay suspension [i.e. TN8, Fig. 5(f)]. This indicates that the shear rate G is the dominant factor controlling aggregation and break-up processes and, hence, the peak floc sizes generated in the column for both kaolin clay and sand-clay mixtures under this high grid-generated shear condition.

3.5 Parametric Controls on Equilibrium Floc Sizes

Examination of the results presented in Figs. 5 and 6 indicate that the temporal variation in the measured in-situ concentration C has a significant parametric influence on temporal variation of the maximal $D_{f,95}$, $D_{f,90}$ and root-mean-square $D_{f,rms}$ floc sizes generated in the settling column. Other parametric controls such as turbulent shear rate G and the presence of a sand fraction in sand-clay mixed suspensions also have a strong influence on both the initial aggregation rates and the quasi-equilibrium floc sizes attained. The relative influence of shear rate G and concentration C on the balance between floc aggregation and break-up processes has been considered previously within a Lagrangian framework derived by Winterwerp [16,35] for mud-only suspensions. With this approach, the equilibrium floc size $D_{f,e}$ (i.e. when aggregation and break-up terms balance in the Lagrangian framework) is defined by:

$$D_{f,e} = \frac{k_A C}{k_B \sqrt{G}} \quad (4)$$

where k_A and k_B are empirically-determined, dimensional aggregation ($\text{m}^2 \text{ kg}^{-1}$) and break-up ($\text{s}^{1/2} \cdot \text{m}^{-2}$) parameters, and C is a representative (and constant) suspended sediment mass concentration. For the current settling column runs with kaolin clay and sand-clay suspensions, the measured maximal $D_{f,95}$, $D_{f,90}$ and root-mean-square $D_{f,rms}$ floc sizes might be expected to scale with $C/G^{1/2}$ (where C is taken as the TSS concentration in the column at OBS₂), once peak or *quasi-equilibrium* floc sizes are attained towards the end of the runs. In the previous experimental study by the authors [3], a general parametric relationship between the peak maximal $D_{f,95}$ floc sizes, the initial “single-shot” clay concentration C_{ini} (g l^{-1}) in the upper buffer tank [Fig. 1(a)] and the grid-generated shear rate G (s^{-1}) was given by:

$$D_{f,95} \propto \frac{C_{ini}^\alpha}{G^\beta} \quad (5)$$

where empirical coefficients $\alpha = 2/5$ and $\beta = 1/2$ for best fit to both the kaolin clay and sand-clay mixture suspension data. In the current study, with continuous kaolin clay (and sand) feed conditions over a finite duration (Table 1), peak or *quasi-equilibrium* floc sizes are generally attained once TSS concentrations (i.e. $C_c + C_s$) in the settling column

approach relatively constant (i.e. equilibrium) values. In this context, Figs. 7(a)-(c) present relationships between the peak or *quasi-equilibrium* floc sizes $D_{f,95}$, $D_{f,90}$ and $D_{f,rms}$ attained for each run and a modified flocculation parameter $(C/G)^{1/2}$ [i.e. where $\alpha = \beta = 1/2$, Eq. (5)], which provides the best fit to both the kaolin clay and sand-clay suspension data. [Note: the horizontal error bars in Fig. 7 represent the standard deviation in the mean in-situ concentrations C measurements over the period of *quasi-equilibrium* conditions, while the vertical error bars represent the standard deviation in calculated representative floc sizes over the same period]. Overall, Figs. 7(a) and (b) indicate good correlation ($R^2 > 0.95$) with a proportionality relationship $D_{f,95}; D_{f,90} \propto (C/G)^{1/2}$ for the majority of kaolin clay and sand-clay runs. The outliers to this relationship occur for runs at higher clay input concentrations, which indicate the formation of smaller $D_{f,95}$ and $D_{f,90}$ flocs sizes than might be expected. At low shear rate conditions, this is in accord with previous findings [32,33] that floc sizes can reduce with increasing mass concentration C due to an increasing influence of floc-floc collisions in the break-up processes relative to turbulent fluid shearing effects. Conversely, under high shear rate conditions, it can also be hypothesized that the $D_{f,95}$ and $D_{f,90}$ floc sizes attained will be strongly controlled by shear-dominated break-up processes and, thus, largely independent of concentration C (and, indeed, the presence of the sand fraction). In terms of the root-mean-square $D_{f,rms}$ floc sizes, Fig. 7(c) shows considerably more scatter in the kaolin clay and sand-clay mixture data, with the proportionality relationship $D_{f,rms} \propto (C_b/G)^{1/2}$ indicating much lower correlation ($R^2 = 0.62$) to this data. This is as expected due to large (and variable) populations of smaller microflocs in the FSDs (Fig. 4) will have a strong influence on the calculated $D_{f,rms}$ values in each run. Finally, it is noted that the peak or *quasi-equilibrium* $D_{f,95}$ floc sizes attained for the sand-clay mixtures are typically lower than the median sand grain size (i.e. $D_{s,50} = 150 \mu\text{m}$), with no indication of macroflocs ($D_f > 150 \mu\text{m}$) present in the FSDs. As such, it is hypothesised that the sand fraction imposes a potential limiting condition on the maximal clay floc sizes attainable within the sand-clay mixtures.

4. Numerical modelling

The flocculation of cohesive sediments can be modelled by either adopting (i) a simple Lagrangian-type floc growth equation [16,35] to predict the temporal evolution of a single characteristic floc size D_f , or (ii) more complex population balance equations (PBEs) [27,44–47], which predict the temporal evolution of the complete floc size distribution (FSD). In terms of the former approach, Eq. (4) describes the characteristic equilibrium floc size $D_{f,e}$ attained under specific environmental conditions (i.e. concentration C and shear rate G), assuming they remain constant for a time period in excess of the flocculation time T_f for the equilibrium floc size $D_{f,e}$ to be reached (i.e. $D_f \rightarrow D_{f,e}$) [48]. A variation on this simple Lagrangian approach has been used above as a first attempt for the interpretation of the *quasi-equilibrium* values of representative floc sizes generated in the settling column runs (Fig. 7). Both the Lagrangian and

PBE modelling approaches can be coupled within a one-dimensional vertical (1DV) numerical model [35,44,46,47] to simulate the spatio-temporal variability in flocculation processes associated with concentration gradients and locally-varying hydrodynamic conditions. In relation to the current experiments, the PBE model approach permits more direct comparisons with the temporal development in the floc size distributions (FSDs) and associated maximal $D_{f,95}$ and root-mean-square $D_{f,rms}$ floc sizes generated in the settling column. It also provides better scope for incorporating size and fractional (i.e. sand-clay) selectivity in the aggregation and break-up terms incorporated in the model. Thus, a simplified 1DV approach (based on solution of the 1DV advection-diffusion equation) is developed herein to incorporate a newly-extended PBE model capable of predicting the flocculation behaviour (i.e. aggregation and break-up) of both the kaolin clay and sand-clay mixture suspensions tested. The key new aspect of this PBE model is an additional break-up term included to account for floc fragmentation mechanisms associated with inter-fractional interactions (i.e. collisions between sand particles and clay flocs collisions) and their influence on the floc growth rates and the maximum floc sizes attained in the settling column runs. To the authors' best knowledge, this is the first time that such multi-fractional (sand-clay) interactions have been included in a PBE model approach.

4.1 1DV advection-diffusion model

The 1DV unsteady advection-diffusion equation for a multi-fractional sediment suspension is given by

$$\frac{\partial C_i}{\partial t} + w_{s,i} \frac{\partial C_i}{\partial z} = \frac{\partial}{\partial z} \left(\Gamma_{s,i} \frac{\partial C_i}{\partial z} \right), \quad (6)$$

where C_i is the mass concentration of individual sediment fractions (i.e. clay flocs or sand particles) in the i^{th} size class; $w_{s,i}$ is the fractional hindered settling velocities, calculated by the expressions of Winterwerp [16] and Cheng [49,50] for clay floc and sand particle fractions, respectively; and $\Gamma_{s,i}$ is the corresponding turbulent diffusion coefficients. Eq. (6) is discretised and solved using a Crank-Nicholson Implicit Scheme with upwind differencing on advection terms and central differencing on diffusion terms to calculate updated fractional mass concentration C_i within cells at different elevations within the column. For application in the settling column, the boundary conditions in the top cell are defined by the temporal variation in the clay concentration C_i within the upper buffer tank (i.e. due to the peristaltic pump feed), as well as the direct dry sand feed rate into the settling column, in order to represent the experimental conditions tested. At the bottom cell, a fully absorbing boundary condition is specified to represent mass loss due to deposition at the column base (Fig. 8).

4.2 Population Balance Equation

The flocculation and break-up behaviour of cohesive (clay) and mixed (sand-clay) suspensions can be simulated using a discretised population balance equation (PBE) approach to account for temporal and spatial variations in the floc size

distribution (FSD) under varying hydrodynamic conditions and suspended sediment concentrations. Within the PBE, the total FSDs are divided into size classes with their temporal evolution characterised by individual balance equations that determine changes in the floc concentrations in each size class due to aggregation (i.e. floc-floc collisions) and break-up processes (i.e. shear-induced floc break-up; sand particle-floc collisions). These discretised PBE approaches also have to ensure that mass conservation is achieved between the different classes, such that the total mass of the FSD is conserved during the simulation. When applied in a 1DV model framework, the PBE approach can be used to predict clay aggregation and break-up processes within the settling column in each discretised cell (Fig. 8) and at each time step. The classical population balance equation given by von Smoluchowski [51] is

$$\frac{dn_k}{dt} = \frac{1}{2} \sum_{i+j=k} \alpha_{i,j} \beta_{i,j} n_i n_j - n_k \sum_{i=1}^{\infty} \alpha_{i,k} \beta_{i,k} n_i \quad (7)$$

which describes the irreversible aggregation rate between flocs of size i and j , forming larger flocs of size k (i.e. where $k = i + j$). Within Eq. (7), $n_{i,j}$ is the number concentration for flocs in size classes i and j , respectively. The first term on the right hand side of Eq. (7) relates to the rate of increase in number concentration n_k resulting from the aggregation of smaller floc sizes i and j , while the second term refers to the rate of reduction in n_k arising from the aggregation of k -sized flocs with all other floc sizes i (including $i = k$). Several assumptions are generally adopted in the von Smoluchowski [51] formulation, including: (i) all floc collisions are successful in leading to aggregation (i.e. collision efficiency $\alpha_{i,j} = 1$); (ii) all particles and flocs within different size classes are considered spherical (i.e. no account of the fractal nature of flocs); and (iii) no aggregate break-up terms are included within the formulation.

In solving Eq. (7), a volume-doubling discretisation $V_{i+1} = 2V_i$ [44,52] is adopted for the clay fraction in order to reduce the number of floc size classes required to cover the floc size distribution (FSD) observed within the experiments. This is also a more computationally efficient approach for solving the FSD at different elevations within the settling column. Within this lumped discretisation, we specify $M (= 30)$ clay size classes, where the geometric diameter D_i of size class i is defined by:

$$D_i = D_1 \left(2^{(i-1)/3} \right) \quad (8)$$

where $D_1 (= 2 \mu\text{m})$ is the diameter of the primary clay particle. This lumped approach allows floc sizes to be generated up to $D = 813 \mu\text{m}$ (at $i = 30$), which is significantly larger than the floc sizes generated within the settling column for either the kaolin clay or sand-clay mixture runs. For the kaolin clay suspensions, the lumped discrete PBE including both aggregation and break-up terms is given in the form

$$\begin{aligned} \frac{dn_i}{dt} = & \sum_{j=1}^{i-2} (1 - f_{i-1,j}) \alpha_{i-1,j} \beta_{i-1,j} n_{i-1} n_j + \frac{1}{2} \alpha_{i-1,i-1} \beta_{i-1,i-1} n_{i-1}^2 - \sum_{j=1}^{i-1} (1 - f_{i,j}) \alpha_{i,j} \beta_{i,j} n_i n_j - \frac{1}{2} \alpha_{i,i} \beta_{i,i} n_i^2 - \\ & \sum_{j=i+1}^M \alpha_{i,j} \beta_{i,j} n_i n_j + \sum_{j=i+1}^M \Gamma_j S_j n_j - S_i n_i \end{aligned} \quad (9)$$

where $\alpha_{i,j}$ is the collision efficiency between floc sizes in classes i and j ; $\beta_{i,j}$ is the collision frequency; $f_{i,j}$ is the size class allocation factor [44]; Γ_i is the floc breakage function; and S_i is the floc fragmentation rate (see section 4.2.1 below). The particle number concentration n_i in each class can be related to the known suspended mass concentration C_i as

$$n_i = \frac{C_i}{\rho_i V_i} \quad (10)$$

where V_i and ρ_i are the representative floc volume and density, respectively, for size class i , where $V_i = f_s D_i^3$ (with f_s being a shape factor set to unity) and ρ_i calculated via [35] as follows

$$\rho_i = \text{smaller of} \left\{ \begin{array}{l} \rho_s \\ \rho_w + (\rho_s - \rho_w) \left(\frac{D_p}{D_i} \right)^{3-n_f} \end{array} \right. \quad (11)$$

where ρ_w and ρ_s are the water and sediment particle densities, respectively, and n_f is the fractal dimension of the flocs (assumed to be $n_f = 2.0$, [48]). Substituting Eq. (11) into Eq. (10) yields:

$$n_i = \frac{6}{\pi} \frac{C_i}{\rho_s} D_p^{n_f-3} D_i^{-n_f} \quad [\text{mud floc classes}] \quad (12)$$

$$n_i = \frac{6}{\pi} \frac{C_i}{\rho_s D_i^3} \quad [\text{sand particle class}] \quad (13)$$

The mass-conserving, lumped PBE solved within each discretised region (Fig. 8) can be derived from Eqs. (9) and (13) (see Appendix 1) to have the expanded form

$$\begin{aligned} \frac{dC_i}{dt} = & \left\{ \sum_{j=1}^{i-2} \rho_j V_j [\Delta n_{i-1}(i-1, j) + \Delta n_j(j, i) - \Delta n_i(i, j)] + \rho_{i-1} V_{i-1} \Delta n_{i-1}(i-1, i-1) + \right. \\ & \left. \rho_{i-1} V_{i-1} \sum_{j=1}^{i-2} \Delta n_{i-1}(i-1, j) + \rho_{i-1} V_{i-1} [\Delta n_{i-1}(i-1, i) - \Delta n_i(i, i-1)] \right\} - \\ & \rho_i V_i \left[\frac{1}{2} \alpha_{i,i} \beta_{i,i} n_i^2 + \sum_{j=1}^{i-1} (1 - f_{i,j}) \alpha_{i,j} \beta_{i,j} n_i n_j + \sum_{j=i+1}^M \alpha_{i,j} \beta_{i,j} n_i n_j \right] + \\ & \left[\rho_i V_i \sum_{j=i+1}^M \Gamma_j S_j n_j \right] - (\rho_i V_i S_i n_i) + \left[\rho_i V_i \sum_{j=i+1}^M \Gamma_j S_{j,M+1} n_j \right] - (\rho_i V_i S_{i,M+1} n_i) \end{aligned} \quad (14)$$

where $\Delta n_i(i, j)$ represents the floc number change in any size class i resulting from collisions leading to aggregation with flocs in any size class j , where, in general

$$\Delta n_i(i, j) = (1 - f_{i,j}) \alpha_{i,j} \beta_{i,j} n_i n_j \quad (15)$$

In this way, the combined terms within the $\{\dots\}$ brackets in Eq. (14) represent the mass increase in size class i due to the combination of smaller flocs [i.e. up to size class $(i - 1)$] with $(i - 1)$ and i size classes. The second combined term in Eq. (14) represents the mass loss in size class i due to the combination of i sized flocs with all floc size classes. The third and fourth terms represent the mass increase and reduction in size class i due to the shear break-up of flocs in larger size classes [i.e. $j = (i + 1) \rightarrow M$] and within size class i itself, respectively. Finally, the fifth and sixth terms represent the new additional break-up mechanism associated with the collision of sand particles [represented as size class $(M + 1)$ in the PBE model] and clay flocs [3], resulting in an increase and reduction of the mass in floc size class i , respectively. This effect of this additional sand-clay break-up mechanism on initial aggregation rates and maximum floc sizes is discussed in more detail later.

4.2.1 PBE model parameters

As the collisions between flocs in the present PBE model are assumed to be binary, the well-established “shell-core” model [53] is employed to estimate the collision efficiency $\alpha_{i,j}$ between two flocs from size classes i and j , such that:

$$\alpha_{i,j} = \left[\frac{\exp\left[-x(1-i/j)^2\right]}{(i \times j)^y} \right] \alpha_{\max} \quad (\text{for } i \geq j) \quad (16)$$

where x and y ($= 0.1$) are fitting parameters and α_{\max} ($= 1.0$) denotes the upper limit of $\alpha_{i,j}$. This semi-empirical model predicts $\alpha_{i,j}$ to be significantly reduced (i.e. $\alpha_{i,j} \rightarrow 0$) when the floc size ratio $D_j/D_i \ll 1$, compared to higher collision efficiencies obtained when $D_i \approx D_j$.

The frequency $\beta_{i,j}$ of the binary collisions between flocs from size classes i and j is estimated from the arithmetic sum of perikinetic interactions due to Brownian motion $\beta_{b(i,j)}$ [44,46], orthokinetic interactions due to shear from the isotropic (i.e. grid-generated) turbulence $\beta_{sh(i,j)}$ [27,45,46], and interactions resulting from differential settling $\beta_{ds(i,j)}$ [46], i.e.

$$\beta_{b(i,j)} = \left(\frac{2k_B T}{3\mu} \right) \frac{(D_i + D_j)^2}{D_i D_j} \quad (17)$$

$$\beta_{sh(i,j)} = \frac{1}{6} G (D_i + D_j)^3 \quad (18)$$

$$\beta_{ds(i,j)} = \left(\frac{\pi}{4} \right) (D_i + D_j)^2 |w_{s,j} - w_{s,i}| \quad (19)$$

$$\beta_{(i,j)} = \beta_{b(i,j)} + \beta_{sh(i,j)} + \beta_{ds(i,j)} \quad (20)$$

Here, k_B is the Boltzmann constant ($= 1.38 \times 10^{-23} \text{ m}^2 \cdot \text{kg} \cdot \text{s}^{-2} \cdot \text{K}^{-1}$); T is the absolute temperature (K); G is the shear rate (s^{-1}); $w_{s,i}$ and $w_{s,j}$ are the settling velocities of fractions i and j , respectively [16]. In dynamic environments, it can be assumed that the collision frequency contribution from Brownian motions $\beta_{b(i,j)}$ is negligible [45] in comparison to the contributions from shear and differential settling.

The size class allocation factor $f_{i,j}$ [44] defines the fraction of newly-formed flocs due to binary collisions are allocated to each size class i to maintain mass-balance within the lumped PBE approach adopted, having the form:

$$f_{i,j} = \frac{\rho_{f,i} V_i + \rho_{f,j} V_j - \rho_{f,i+1} V_{i+1}}{\rho_{f,i} V_i - \rho_{f,i+1} V_{i+1}} \quad (21)$$

In terms of the floc break-up characteristics due to shear, a binary breakage model is assumed, within which two equal-sized flocs are assumed to form from the break-up of larger aggregates [i.e. breakage coefficient $\Gamma = V_i / V_{i+1}$ ($= 1/2$) within the volume-doubling discretisation adopted]. The fragmentation rate coefficient S_i for flocs i is estimated by the semi-empirical expression proposed by [53], i.e.

$$S_i = \left(\frac{4}{15\pi} \right)^{1/2} G^{1/2} \exp \left(\frac{-\varepsilon_{bi}}{G^2 \nu} \right) \quad (22)$$

where $\varepsilon_{bi} = B/R_{ci}$ is the critical energy dissipation that causes floc break-up; B is the empirical break-up fitting parameter that allows fewer or more floc break-ups at a given size class i ; R_{ci} is effective capture radius of the floc in size class i . As such, the fragmentation rate S_i is largely determined by the floc geometry in size class i and the level of turbulent shear it is exposed to.

The final two terms as defined in Eq. (14) account for the new floc break-up mechanisms associated with direct collisions and indirect interactions between flows and sand particles. It is important to emphasise here that the microscale dynamics of the polydisperse, inter-fractional (sand-clay) interactions could not be determined explicitly from the experimental data obtained in the settling column runs with sand-clay mixtures. As such, these multi-fractional interactions are assumed to be represented by sand particle-clay floc collisions within the new extended PBE model, in a same manner to the treatment of floc-floc collisions that result in aggregation [3], but instead these particle-floc collisions result in floc fragmentation. Analysis of the experimental data for the sand-clay mixtures also indicated that the peak or *quasi-equilibrium* maximal $D_{f,95}$ floc sizes attained in the settling column were generally smaller than the mean sand particle size ($D_{s,50} = 150 \mu\text{m}$), with no evidence of macroflocs ($D_f > 150 \mu\text{m}$) being generated in these runs.

As such, it is assumed that floc fragmentation resulting from sand particle – clay floc collisions occurs only for floc size classes i larger than the sand particles (i.e. $D_i \geq D_{s,50} = 150 \mu\text{m}$) and results in a binary floc breakage (i.e. $\Gamma_{i+1} = 1/2$; $V_{i+1} \rightarrow 2V_i$), with the fragmentation coefficient $S_{i,M+1}$ thus defined as follows

$$S_{i,M+1} = \alpha_{i,M+1} \beta_{i,M+1} n_{M+1} \quad (23)$$

With no available knowledge on the inter-factional (sand-clay) collision efficiency $\alpha_{i,M+1}$, it is assumed to satisfy the following simple relationship:

$$\alpha_{i,M+1} = \begin{cases} 0 & D_i < D_{s,50} \\ \text{const.} & D_i \geq D_{s,50} \end{cases} \quad (24)$$

It is also proposed that the inter-factional (sand-clay) collision frequency $\beta_{i,M+1}$ can be defined by Eqs. (17) – (20), through the substitutions $D_j = D_s$ and $w_{s,j} = w_{s,M+1}$ to account for different mechanisms most likely to lead to these inter-factional collisions (e.g. turbulent shear and differential settling).

4.3 Comparison between Experimental and 1DV PBE Model Results

For direct comparisons with the laboratory data collected in the kaolin clay and sand-clay mixture settling column runs, it is necessary to incorporate a number of idealisations and simplifications in the 1DV PBE model simulations to represent the prevalent experimental conditions. Firstly, the temporal variation in the clay concentration at the upper model boundary cell $k = 1$ of the 1DV model domain (Fig. 8) is represented by specifying accurately (i) the inflow rate Q_m , concentration C_m and duration t_m from the peristaltic pump feed into the upper buffer mixing tank (see Table 1); (ii) the buffer tank volume V_{buff} ; (iii) a mass transfer rate of kaolin clay from the tank into the main column section; and (iv) the mass loss from the buffer tank via the overflow pipe. Secondly, as no information is available on the initial floc size distribution (FSD) generated in the buffer tank, it is assumed that the initial clay size specified in cell $k = 1$ is set to the primary particle size $D_p = 2 \mu\text{m}$. This is very conservative as some degree of clay flocculation would be expected to occur in the paddle-stirred buffer tank (Fig. 1) prior to transfer into the main column section,. Thirdly, the sand input concentration into the upper column is applied directly in cell $k = 1$ through the dry feed rates I_s (Table 1) and cell volume $V_{k=1}$, assuming a uniform sand particle size $D_s = 150 \mu\text{m}$. Finally, in the main column section, the grid-stirred turbulence intensities and corresponding shear rates G are shown to increase significantly as the individual oscillating grids are approached [Eq. (2) and Table 1]. In the 1DV PBE model simulations, this spatial variability in grid-generated turbulence is ignored, with uniform G values specified in the 1DV model domain (Fig. 8) for each different experimental condition.

A limited number of experimental runs with kaolin clay (TN4, TN5, TN7 and TN8; Table 1] and sand-clay mixture (TNS2, TNS5 and TNS6; Table 1) suspensions are modelled, enabling parametric sensitivity to variations in grid shear rate G , clay input concentration C_m and the presence of sand to be investigated. The key 1DV PBE model parameters specified for each kaolin clay and sand-clay mixture run are summarised in Table 2, along with details of the PBE model coefficients that remain consistent over all simulations. Key parameters that have been included in the extended PBE [Eq. (14)] to reflect the influence of the sand fraction on the aggregation and break-up of clay flocs include the sand particle-floc collision efficiency $\alpha_{i,M+1}$ [Eq. (24)], which is set at 0.5 for floc sizes $D_f \geq 150 \mu\text{m}$. The settling velocity $w_{s,M+1}$ of the sand particles, used in Eq. (19) to predict the effect of differential settling on collision frequency β_{ds} , is also calculated from established formulae [49,50]. The 1DV PBE model simulations for both the kaolin clay and sand-clay mixture runs are therefore compared directly with the experimental data on (1) total mass concentrations $TSS = C_c + C_s$ in model cells (i.e. $k = 15$ and 30 , respectively, Fig. 8) equivalent to the OBS_1 and OBS_2 positions; and (2) initial aggregation rates and the peak or *quasi-equilibrium* maximal $D_{f,95}$ and root-mean-square $D_{f,rms}$ floc sizes attained at the bottom of the 1DV model domain (i.e. cell $k = 30$, Fig. 8). As such, the experimental data from the settling column runs is used here primarily to verify the aggregation and break-up terms specified in the new extended PBE model, which isolate the quantitative contributions to flocculation behaviour from floc growth (i.e. due to floc-floc collisions) and break-up (i.e. due to shear induced floc breakage and sand particle-floc collisions).

Fig. 9 presents comparisons between 1DV PBE model simulations and experimental measurements for the kaolin clay runs outlined above. Figs. 9(a1)-(d1) indicate that the 1DV advection-diffusion model predicts well the rate of increase in clay concentration C_c at both column elevations over the duration of clay input into the buffer tank ($t_m = 152 - 192$ mins, Table 1). The observed temporal lag in the concentration increase at the bottom of the column (i.e. OBS_2 , cell $k = 30$) compared to at the mid-elevation (i.e. OBS_1 , cell $k = 15$) is also predicted by the 1DV model, although the predicted concentration differential between the two positions is, in general, lower than measured in the column. This discrepancy is likely to be due to assumptions associated with the diffusive behaviour of clay suspensions, especially the assumption of a constant diffusion coefficient $\Gamma_{s,i} = 50 \times 10^{-5} \text{ m}^2 \text{ s}^{-1}$ in Eq. (6) (see Table 2) for all clay floc size classes and at all column elevations. The 1DV model predictions indicate correctly the measured adjustment to quasi-steady concentration values [i.e. $C_c \rightarrow \sim 0.6 \text{ g l}^{-1}$ and $\sim 0.9 \text{ g l}^{-1}$ in Figs. 9(a1),(c1) and 9(b1),(d1) for clay input concentrations $C_m = 1.2 \text{ g l}^{-1}$ and 1.8 g l^{-1} , respectively] at OBS_1 and OBS_2 positions following the cessation of the clay feed into the buffer tank. Indeed, both measured and predicted concentrations at OBS_1 indicate a slight reduction at later stages of the runs due to the gradual decrease in buffer tank concentrations after the clay input has ceased. Overall, the level of

agreement between the 1DV model and experimental data for temporally-varying clay concentrations at OBS₁ (i.e. cell $k = 15$) and OBS₂ (i.e. cell $k = 30$) is relatively good given the simplifications and assumptions imposed in the model.

Figs. 9(a2)-(d2) show the PBE model predictions of the temporally-varying maximal $D_{f,95}$ and root-mean-square $D_{f,rms}$ floc sizes at the bottom of the 1DV model domain (i.e. cell $k = 30$, Fig. 8), compared to the experimental floc data for the kaolin clay settling column runs. It is noted here that the model predictions of $D_{f,95}$ floc sizes show discontinuities along the time series, which arise from the size class discretisation of the floc size distribution (FSD) in the PBE approach. Comparing Figs. 9(a2) and (b2) (i.e. runs TN4 and TN5, respectively – see Tables 1 and 2), it is observed that the initial aggregation rate is higher for the higher clay input condition [i.e. TN5: $C_m = 1.8 \text{ g l}^{-1}$, Fig. 9(b2)] in agreement with the experimental findings. Indeed, the mean aggregation rates $dD_{f,95}/dt$ for the model simulations can be estimated over the same initial aggregation phase as shown in Figs. 5(c) and (d) (i.e. best-fit trend lines to initial increasing $D_{f,95}$ floc measurements). These model predicted aggregation rates of $dD_{f,95}/dt = 0.42 \text{ } \mu\text{m}/\text{min}$ for TN4 [i.e. Fig. 9(a2)] and $0.60 \text{ } \mu\text{m}/\text{min}$ [i.e. Fig. 9(b2)], compare favourably with the measured aggregation rates $D_{f,95}/dt = 0.37 \text{ } \mu\text{m}/\text{min}$ and $0.66 \text{ } \mu\text{m}/\text{min}$ [i.e. Figs. 5(c) and (d), respectively]. In both runs, however, the predicted maximal $D_{f,95}$ and root-mean-square $D_{f,rms}$ floc sizes are significantly lower than the measured floc sizes during this initial aggregation phase. This is due largely to the conservative upper boundary condition in the 1DV PBE model, where an initial floc size $D_f = 2 \text{ } \mu\text{m}$ is specified at cell $k = 1$ (Fig. 8). This effect is also clearly highlighted in Figs. 9(c) and (d) for the high shear simulations of runs TN7 and TN8, respectively (see Tables 1 and 2). Here, the initial aggregation phases predicted by the model simulations are not shown in the corresponding experimental data, where measured $D_{f,95}$ and $D_{f,rms}$ floc sizes remain relatively constant throughout the run durations. In all 1DV PBE simulations for kaolin clay suspensions [Figs. 9(a2) – (d2)], after this initial aggregation phase, the subsequent temporal development of $D_{f,95}$ and $D_{f,rms}$ floc sizes diminishes (i.e. $dD_f/dt \rightarrow 0$) as the flow sizes approach quasi-equilibrium values. This occurs at elapsed times coinciding approximately with the development of equilibrium concentrations at both cells $k = 15$ (i.e. OBS₁) and $k = 30$ (i.e. OBS₂) within the 1DV domain. In all cases, these predicted equilibrium $D_{f,95}$ and $D_{f,rms}$ floc sizes correspond well with the peak or *quasi-equilibrium* floc sizes measured in the settling column during the later stages of experimental runs [Figs. 9(a2) – (d2)]. This is illustrated in Table 3 where relative differences between the 1DV PBE predictions and measurements of $D_{f,95}$ and $D_{f,rms}$ floc sizes are less than 10%.

In terms of the model simulations for the sand-clay mixture runs, Fig. 10(a)-(c) present corresponding time series of the predicted and measured maximal $D_{f,95}$ and root-mean-square $D_{f,rms}$ floc sizes for runs TNS2, TNS5 and TNS6, respectively (see Tables 1 and 2). In accord with the kaolin clay simulations, the model predictions of $D_{f,95}$ and $D_{f,rms}$

floc sizes during the initial aggregation phase are generally lower than the measurements [see Fig. 10(b) and (c)], again due to the specification of a conservative initial floc size ($D_f = 2 \mu\text{m}$) condition at the upper boundary (i.e. $k = 1$, Fig. 8) in the 1DV PBE model. However, subsequent to this initial aggregation phase, the predicted $D_{f,95}$ and $D_{f,rms}$ floc sizes approach quasi-equilibrium values, which are again in good agreement with experimental data (see Table 3), with relative differences between measured and predicted floc sizes lower than 10%, as for the kaolin clay runs.

It is noted that for both these kaolin clay and sand-clay mixture simulations some adjustment of the floc break-up parameter B (Table 2), required for the critical energy dissipation ε_{bi} term in the floc fragmentation rate S_i parameter [Eq. (22)], is required to improve the fit to experimental data. When combined with the newly-defined fragmentation coefficient $S_{i,M+1}$ for sand particle – clay floc collisions, it is acknowledged that some uncertainty remains as to how best to define these empirical coefficients and parameters in the multi-fractional PBE model. As such, it is useful to compare 1DV PBE model simulations for equivalent kaolin clay and sand-clay suspensions (under otherwise identical parametric conditions) to determine the relative influence of the fragmentation parameters S_i and $S_{i,M+1}$ on both the initial aggregation rates and the quasi-equilibrium floc sizes attained. In this regard, Fig. 11(a) shows comparative simulations for TN5 (kaolin clay) and TNS5 (sand-clay) runs under medium shear conditions (Table 1). With the floc break-up parameter $B = 2.5$ specified in both runs [i.e. black and blue traces, Fig. 11(a)], it is apparent that the additional break-up effects due to sand particle – clay floc collisions in the TNS5 simulation reduces both the initial aggregation rate and quasi-equilibrium floc sizes attained (i.e. $D_{f,95} = \sim 165 \mu\text{m} \rightarrow \sim 150 \mu\text{m}$; $D_{f,rms} = \sim 82 \mu\text{m} \rightarrow \sim 72 \mu\text{m}$), in general accord with the experimental measurements (Table 3). However, to gain improved agreement with the TNS5 floc size data, the break-up parameter $B = 3.0$ is used [see Fig. 10(b)], which results in a higher initial aggregation rate and lower quasi-equilibrium maximal floc size $D_{f,95} = \sim 140 \mu\text{m}$ [i.e. green trace, Fig. 11(a)]. In Fig. 11(b), which compares simulations for TN8 (kaolin clay), TNS2 (sand-clay) and TNS6 (sand-clay) runs under high shear conditions (Table 1), it is clear that the influence of the sand particle – clay floc collisions (i.e. through fragmentation rate $S_{i,M+1}$) is significantly diminished compared to under the medium shear conditions [Fig. 11(a)]. Specifically, the $D_{f,95}$ and $D_{f,rms}$ floc size traces for TN8 and TNS2 almost coincide [i.e. black and blue traces, Fig. 11(b)], with $D_{f,95}$; $D_{f,rms} \rightarrow \sim 118 \mu\text{m}$; $\sim 66 \mu\text{m}$, respectively. For the TNS6 simulation, by specifying floc break-up parameter $B = 3.5$ [i.e. green trace, Fig. 11(b)], an initial higher aggregation rate diminishes quickly and the overall peak maximal floc size is reduced [i.e. $D_{f,95} \rightarrow \sim 113 \mu\text{m}$], with $D_{f,rms}$ remaining largely unchanged.

5. Concluding Remarks

A combined experimental and numerical modelling study has been undertaken to investigate the flocculation behaviour of purely-cohesive (i.e. kaolin clay) and mixed (i.e. sand-clay) sediment suspensions. The experiments were conducted in a grid-stirred settling column, with controlled hydrodynamic conditions generated by a rigid array of oscillating grids. Continuous measurements of total suspended sediment (TSS) concentration were obtained via calibrated OBS probes located at the mid-height (OBS₁) and bottom (OBS₂) of the main column section. Floc size distributions (FSDs) were measured optically, with individual floc diameters D_f calculated via ImageJ image analysis software. Statistical analysis of the floc populations allowed maximal $D_{f,95}$, $D_{f,90}$ and root-mean-square $D_{f,rms}$ floc sizes to be calculated at different stages throughout each experimental run, allowing parametric correlations with in-situ TSS concentrations and turbulent shear rates to be investigated.

Temporal variations in the $D_{f,95}$, $D_{f,90}$ and $D_{f,rms}$ floc sizes for the kaolin clay suspensions indicated that both the aggregation rates and peak floc sizes attained in the column were controlled primarily by the turbulent shear rate G and temporally-varying clay concentrations C_c . Specifically, for low to medium shear rate conditions, the initial aggregation rates for maximal floc sizes ($dD_{f,95}/dt$) and quasi-equilibrium floc sizes attained were shown to increase with clay input concentration C_c (for a given shear rate G), with maximal floc sizes $D_{f,95}$ typically in the macrofloc size range (i.e. $D_f > 150 \mu\text{m}$), although reducing slightly at later stages in the runs. These quasi-equilibrium floc sizes typically coincided with equilibrium clay concentrations being attained at OBS₁ and OBS₂ positions in the column (Fig. 1). For higher shear rate conditions, there was no obvious initial aggregation phase, with representative floc sizes ($D_{f,95}$, $D_{f,90}$ and $D_{f,rms}$) remaining largely unchanged and within the microfloc size range ($D_f < 150 \mu\text{m}$) over the run durations.

The addition of the fine sand fraction to the kaolin clay suspensions was typically shown to reduce both the initial aggregation rates and peak or quasi-equilibrium floc sizes attained for given sand and clay input conditions under low to medium shear rates. In general, very few macroflocs ($D_f > 150 \mu\text{m}$) were generated within these sand-clay mixtures, suggesting that the presence of the fine sand inhibits flocculation either through direct inter-fractional (sand-clay) collisions and/or induced shear due to differential settling effects, as initially hypothesised by Cuthbertson et al. [3]. By contrast, under higher shear rate conditions, the representative floc sizes ($D_{f,95}$, $D_{f,90}$ and $D_{f,rms}$) were largely similar to those generated in equivalent kaolin clay runs, suggesting the influence of sand-clay interactions in controlling aggregation and break-up processes is diminished in comparison to the dominant influence of high grid-generated turbulent shear. The parametric controls on the peak or quasi-equilibrium $D_{f,95}$ and $D_{f,90}$ floc sizes for both kaolin clay and sand-clay mixtures indicated direct proportionality to a modified flocculation parameter $(C/G)^{1/2}$, with a few

outliers occurring at (i) low shear rates, where high concentrations C can promote floc-floc collisions leading to floc breakage, or (ii) high shear rates, where shear-induced floc breakage is largely independent of concentration.

A discretised 1DV PBE model was developed to simulate the temporally-varying flocculation behaviour of both the kaolin clay and sand-clay suspensions within the settling column runs. The key new aspect of this numerical study was the inclusion of additional floc break-up terms to account for multi-fractional (sand-clay) collisions and their effect on aggregation rates and the maximum floc sizes attained in the sand-clay mixture runs. This was based mainly on the experimental observation that very few macroflocs ($D_f > 150 \mu\text{m}$) were measured in the sand-clay runs compared to pure kaolin clay suspensions, where maximal sizes $D_{f,95}$ often exceeded this threshold. As such, it was hypothesised that the break-up of flocs due to sand-clay collisions would only occur in the macrofloc size range and can be treated in the PBE in a similar manner to the floc-floc collisions that lead to aggregation. It is acknowledged here, however, that this is a first attempt to include the influence of sand-clay interactions on the aggregation and break-up characteristics of mixed (sand-clay) suspensions and, thus more precise details of the fundamental microphysics of these interactions, and their consequences, are required to improve their future representation in PBE-type models.

Model simulations of both the kaolin clay and sand-clay suspensions in general provided good agreement with the experimental measurements of peak or quasi-equilibrium $D_{f,95}$, $D_{f,90}$ and $D_{f,rms}$ floc sizes, although this was somewhat dependent on the specification of appropriate break-up terms to represent the shear-induced S_i and sand-clay collision-induced $S_{i,M+1}$ floc fragmentation rates. Furthermore, a general discrepancy between measured and predicted $D_{f,95}$ and $D_{f,rms}$ floc sizes during the initial aggregation phase (i.e. with PBE simulations generally under-predicting floc sizes) was due largely to the implicit assumption of an unflocculated clay fraction (i.e. $D_f = D_p = 2 \mu\text{m}$) at the upper boundary of the 1DV model domain. The validity of this assumption could have been tested by measuring the FSD in the buffer tank to provide a more appropriate upper boundary condition within the PBE model. However, as an example, Fig. 11(c) shows an additional 1DV PBE simulation for kaolin clay run TN4 (Table 1) within which an initial floc size $D_f = 40 \mu\text{m}$ is specified in cell $k = 1$ (Fig. 8). When compared with the experimental floc measurements for run TN4, the predicted $D_{f,95}$ and $D_{f,rms}$ floc sizes for this adjusted boundary condition show generally improved agreement during the aggregation phase (as expected), but poorer agreement with peak or quasi-equilibrium floc sizes later in the run. Overall, the combined influence of the shear-induced break-up rates S_i and sand particle – clay floc collision rates $S_{i,M+1}$ in the 1DV PBE model can be summarised as follows: (i) under low-medium shear conditions, the floc break-up rates $S_{i,M+1}$ due to sand-clay collisions have a significant effect in reducing both the initial aggregation rate and peak or quasi-equilibrium floc sizes attained; while (ii) under high shear conditions, the dominance of the shear-induced floc

fragmentation rate S_i , which largely precludes the formation of macroflocs ($D_f > 150 \mu\text{m}$), thus diminishes the effect of the floc fragmentation rate $S_{i,M+1}$ due to absence of sand-macrofloc collisions. A more comprehensive study of these floc break-up processes requires detailed microscale investigations of the particle-floc-fluid interactions and resulting floc fragmentation mechanisms, which is beyond the scope of the current paper.

Acknowledgements

This work was supported by RCUK funding through the Engineering and Physical Sciences Research Council (EPSRC) First Grant Scheme (grant no. EP/K015117/1). Datasets from this study are available upon request from the lead author (a.cuthbertson@hw.ac.uk). The authors are also grateful to the two anonymous reviewers whose invaluable comments have led to significant improvements in the manuscript.

Appendix 1: Derivation of the mass-conserving, lumped PBE model

In the derivation of Eq. (14) from Eqs. (9) – (13), an initial distribution of mass concentration C_i within the different clay floc size classes i (i.e. total number of clay floc size classes $M = 30$) is considered. A PBE flocculation model is then derived to calculate changes to the mass concentrations C_i within each clay floc size class following aggregation mechanisms arising from clay particle-floc and floc-floc collisions and break-up mechanisms associated with turbulent shear and clay floc collisions with sand particles (i.e. specified as size class $M+1$, where relevant).

Firstly, the increase in C_i arising from the aggregation of smaller floc sizes $j = 1$ up to $(i-2)$ with flocs in the $(i-1)$ size class is given by the summation of

$$\Delta C_i(j, i-1) = \left[\sum_{j=1}^{i-2} \rho_j V_j \Delta n_{i-1}(i-1, j) \right] \Delta t, \text{ and} \quad (\text{A1})$$

$$\Delta C_i(i-1, j) = \left[\rho_{i-1} V_{i-1} \sum_{j=1}^{i-2} \Delta n_{i-1}(i-1, j) \right] \Delta t \quad (\text{A2})$$

where ρ and V are the density and volume of flocs within a specific class, and $\Delta n_{i-1}(i-1, j)$ is the change in number concentration in size class $(i-1)$, given by the expression

$$\Delta n_{i-1}(i-1, j) = (1 - f_{i-1, j}) \alpha_{i-1, j} \beta_{i-1, j} n_{i-1} n_j \quad (\text{A2})$$

Here, $\alpha_{i,j}$, $\beta_{i,j}$ and $f_{i,j}$ are defined as the collision efficiency, collision frequency and class allocation coefficients, respectively (see Section 4.2.1). Similarly, the increase in C_i arising from aggregation of smaller floc sizes $j = 1$ up to $(i-2)$ with flocs in the i size class is given by

$$\Delta C_i(j, i) = \left[\sum_{j=1}^{i-2} \rho_j V_j [\Delta n_j(j, i) - \Delta n_i(i, j)] \right] \Delta t, \quad (\text{A3})$$

with $\Delta n_j(j, i)$ and $\Delta n_i(i, j)$ are given by the expressions:

$$\Delta n_j(j, i) = (1 - f_{j, i}) \alpha_{j, i} \beta_{j, i} n_i n_j, \text{ and} \quad (\text{A4})$$

$$\Delta n_i(i, j) = (1 - f_{i, j}) \alpha_{i, j} \beta_{i, j} n_i n_j. \quad (\text{A5})$$

The increase in C_i through aggregation of $(i-1)$ particles with other $(i-1)$ particles is also written as

$$\Delta C_i(i-1, i-1) = [\rho_{i-1} V_{i-1} \Delta n_{i-1}(i-1, i-1)] \Delta t, \quad (\text{A6})$$

with $\Delta n_{i-1}(i-1, i-1)$ is given by

$$\Delta n_{i-1}(i-1, i-1) = \frac{1}{2} \alpha_{i-1, i-1} \beta_{i-1, i-1} n_{i-1}^2. \quad (\text{A7})$$

Finally, in terms of aggregation, the increase in C_i through aggregation of $(i-1)$ particles with i particles is written as

$$\Delta C_i(i-1, i) = \{\rho_{i-1} V_{i-1} [\Delta n_{i-1}(i-1, i) - \Delta n_i(i, i-1)]\} \Delta t, \quad (\text{A8})$$

where $\Delta n_{i-1}(i-1, i)$ and $\Delta n_i(i, i-1)$ are given by

$$\Delta n_{i-1}(i-1, i) = (1 - f_{i-1, i}) \alpha_{i-1, i} \beta_{i-1, i} n_{i-1} n_i \quad (\text{A9})$$

$$\Delta n_i(i, i-1) = (1 - f_{i, i-1}) \alpha_{i, i-1} \beta_{i, i-1} n_i n_{i-1} \quad (\text{A10})$$

By contrast, a decrease in the mass concentration C_i will also occur as a result of the aggregation of i sized particles with all other floc size classes $j = 1$ up to M . This again can be discretised as follows

$$\Delta C_i(i, j) = \rho_i V_i \left[\Delta n_i(i, i) + \sum_{j=1}^{i-1} \Delta n_i(i, j) + \sum_{j=i+1}^M \Delta n_i(i, j) \right] \Delta t. \quad (\text{A11})$$

In terms of floc disaggregation or break-up processes, the increase in mass concentration C_i as a result of the break-up of larger flocs $j = i+1$ up to M can be written in the form

$$\Delta C_i(j) = \left[\rho_i V_i \sum_{j=i+1}^M \Gamma_j S_j n_j \right] \Delta t, \quad (\text{A12})$$

where Γ_j is the breakage distribution function and S_j is the fragmentation parameter (see section 4.2.1). There is also a decrease in mass concentrations C_i resulting from the break-up of flocs in size class i , i.e.

$$\Delta C_i(i) = (\rho_i V_i S_i n_i) \Delta t \quad (\text{A13})$$

When the sand size class $M+1$ is added to the clay floc size classes, it can be assumed that collisions between sand particles and clay flocs from size class i will result in fragmentation into smaller flocs, with the sand fraction remaining as single discrete particles. Assuming that the efficiency α_{ij} and frequency β_{ij} of these collisions are defined in a similar manner to those for floc-floc collisions (see Section 4.2.1), the reduction in mass concentration ΔC_i due to these collisions can be written in the form:

$$\Delta C_i(i) = (\rho_i V_i S_{i, M+1} n_i) \Delta t \quad (\text{A14})$$

where $S_{i, M+1}$ is the fragmentation parameter of flocs in size class i due to collisions with the sand particles ($M+1$), which is assumed to have the following form:

$$S_{i, M+1} = \alpha_{i, M+1} \beta_{i, M+1} n_{M+1} \quad (\text{A15})$$

The corresponding increase in C_i resulting from the break-up of larger flocs $j (= i+1 \rightarrow M)$ following collisions with the sand fraction ($M+1$) can be similarly written as

$$\Delta C_i(j) = \left[\rho_i V_i \sum_{j=i+1}^M \Gamma_j S_{j, M+1} n_j \right] \Delta t \quad (\text{A16})$$

The mass-conserving, lumped PBE shown in Eq. (14) therefore includes all these individual ΔC_i contributions, solving them for each floc size class i and within each discretised region of the modelled settling column (Fig. 8).

References

- [1] R.J. Uncles, J.A. Stephens, C. Harris, Properties of suspended sediment in the estuarine turbidity maximum of the highly turbid Humber Estuary system, UK, *Ocean Dynamics* 56 (2006) 235–247.
- [2] A.J.S. Cuthbertson, S. King, P. Dong, P. A. Davies, Hindered settling velocity of cohesive / non-cohesive sediment mixtures, *Coastal Engineering*, 55(12) (2008) 1197–1208.
- [3] A.J.S. Cuthbertson, P. Dong, P.A. Davies, Non-equilibrium flocculation characteristics of fine-grained sediments in grid-generated turbulent flow, *Coastal Engineering*, 57(4) (2010) 447–460.
- [4] A.J.S. Cuthbertson, O. Ibikunle, W.J. McCarter, G. Starrs, Monitoring and characterisation of sand-mud sedimentation processes, *Ocean Dynamics*, 66(6) (2016) 867–891.
- [5] R. Whitehouse, R. Soulsby, W. Roberts, H. Mitchener, Dynamics of estuarine muds. A manual for practical applications, Thomas Telford Publishing, London, 2000.
- [6] H.J. Williamson, Tidal transport of mud/sand mixtures: Sediment distributions – a literature review, HR Wallingford, Report SR 286, 1991.
- [7] T.J. Chesher, M.C. Ockenden, Numerical modelling of mud and sand mixtures, in: Burt, Parker, Watts (Eds.), *Cohesive Sediments*, John Wiley and Sons, 1997, pp. 395-406.
- [8] M. van Ledden, A process-based sand-mud model, in: J.C. Winterwerp and C. Kranenburg (Eds.), *Fine Sediment Dynamics in the Marine Environment - Proc. in Mar. Science 5*, Amsterdam: Elsevier, 2002, pp. 577-594.
- [9] M. van Ledden, Sand-Mud Segregation in Estuaries and Tidal Basins, PhD thesis, T U Delft, The Netherlands, 2003, 248p.
- [10] B. Waeles, P. Le Hir, P. Lesueur, N. Delsinne, Modelling sand/mud transport and morphodynamics in the Seine river mouth (France): an attempt using a process-based approach, *Hydrobiologia*, 588(1) (2007) 69–82.
- [11] L.P. Sanford, Modeling a dynamically varying mixed sediment bed with erosion, deposition, bioturbation, consolidation, and armouring, *Computers and Geosciences*, 34(10) (2008) 1263–1283.
- [12] P. Le Hir, F. Cayocca, B. Waeles, Dynamics of sand and mud mixtures: A multiprocess-based modelling strategy, *Continental Shelf Research*, 31(10) (2011) S135–S149.
- [13] A.J. Manning, J.R. Spearman, R.J.S. Whitehouse, E.L. Pidduck, J.V. Baugh, K.L. Spencer, Flocculation Dynamics of Mud: Sand Mixed Suspensions, in: A.J. Manning (ed.), *Sediment Transport Processes and Their Modelling Applications*, InTech, 2013, pp. 119-164.

- [14] P.-Y. Burban, W. Lick, J. Lick, The flocculation of fine-grained sediments in estuarine waters, *Journal of Geophysical Research*, 94 (1989) 8323–8330.
- [15] K.R. Dyer, A.J. Manning, Observation of the size, settling velocity and effective density of flocs and their fractal dimensions, *Journal of Sea Research*, 41 (1999) 87–95.
- [16] J.C. Winterwerp, On the flocculation and settling velocity of estuarine mud, *Continental Shelf Research*, 22 (2002) 1339–1360.
- [17] R.B. Krone, A study of rheological properties of estuarial sediments, Report No. 63–68, Hyd. Eng. Lab. and Sanitary Eng. Lab. University of California, Berkeley, 1963.
- [18] D. Eisma, Flocculation and de-flocculation of suspended matter in estuaries, *Netherlands Journal of Sea Research*, 20(2/3) (1986) 183–199.
- [19] A.J. Manning, A study of the effects of turbulence on the properties of flocculated mud, Ph.D. Thesis, Institute of Marine Studies, University of Plymouth, 2001, 282p.
- [20] T.G. Milligan, P.S. Hill, A laboratory assessment of the relative importance of turbulence, particle composition, and concentration in limiting maximal floc size and settling behaviour, *Journal of Sea Research*, 39 (1998) 227–241.
- [21] W. Van Leussen, Aggregation of particles, settling velocity of mud flocs: a review, in: J. Dronkers, W.Ž. van Leussen, (Eds.), *Physical Processes in Estuaries*, Springer, Berlin, 1988, pp. 347–403.
- [22] K. Krank, T.G. Milligan, Characteristics of suspended particles at an 11 hour anchor station in San Francisco Bay, *Journal of Geophysical Research*, 97 (1992) 11373–11382.
- [23] P.T. Spicer, S.E. Pratsinis, Shear induced flocculation: the evolution of floc structure and shape of the size distribution at steady state, *Water Research*, 50 (1996) 1049–1056.
- [24] A.J. Manning, K.R. Dyer, A laboratory examination of floc characteristics with regard to turbulent shearing, *Marine Geology*, 160 (1999) 147–170.
- [25] R. Verney, R. Lafite, J. Claude Brun-Cottan, P. Le Hir, Behaviour of a floc population during a tidal cycle: Laboratory experiments and numerical modelling, *Continental Shelf Research*, 31(10) (2011) S64–S83.
- [26] A. Keyvani, K. Strom, Influence of cycles of high and low turbulent shear on the growth rate and equilibrium size of mud flocs, *Marine Geology*, 354 (2014) 1–14.
- [27] F. Mietta, C. Chassagne, R. Verney, J.C. Winterwerp, On the behavior of mud floc size distribution: model calibration and model behaviour, *Ocean Dynamics*, 61(2-3) (2010) 257–271.
- [28] P. Hill, Controls on floc size in the sea, *Oceanography*, 11(2) (1998), 13–18.
- [29] V. Oles, Shear-induced aggregation and breakup of polystyrene latex particles, *Journal of Colloid and Interface Science*, 154 (1992) 351–358.

- [30] D. Eisma, A. Li, Changes in suspended-matter floc size during the tidal cycle in the Dollard estuary, Netherlands Journal of Sea Research, 31 (1993) 107–117.
- [31] W.B.M. ten Brinke, In situ aggregate size and settling velocity in the Oosterschelde tidal basin (The Netherlands), Netherlands Journal of Sea Research, 32 (1994) 23–35.
- [32] C.H. Tsai, S. Iacobellis, W. Lick, Flocculation of fine-grained lake sediments due to uniform shear stress, Journal of Great Lakes Research, 13 (1987) 135–146.
- [33] W. Lick, J. Lick, Aggregation and disaggregation of fine-grained lake sediments, Journal of Great Lakes Research 14 (1988) 514–523.
- [34] N. Gratiot, A.J. Manning, An experimental investigation of floc characteristics in a diffusive turbulent flow, Journal of Coastal Research, (Special Issue 41) (2004) 105–113.
- [35] J.C. Winterwerp, A simple model for turbulence induced flocculation of cohesive sediment, J. Hydraul. Eng., 36 (3) (1998) 309–326.
- [36] A.J. Manning, J.V. Baugh, J.R. Spearman, R.J.S. Whitehouse, Flocculation settling characteristics of mud: sand mixtures, Ocean Dynamics, 60(2) (2010) 237–253.
- [37] A.J. Manning, J.V. Baugh, J.R. Spearman, E.L. Pidduck, R.J.S. Whitehouse, The settling dynamics of flocculating mud-sand mixtures: Part 1—Empirical algorithm development, Ocean Dynamics, 61(2-3) (2011) 311–350.
- [38] A.J. Manning, S.J. Bass, K.R. Dyer, Floc properties in the turbidity maximum of a mesotidal estuary during neap and spring tidal conditions, Marine Geology, 235(1-4) (2006) 193–211.
- [39] S.M. Thompson, J.S. Turner, Mixing across an interface due to turbulence generated by an oscillating grid, Journal of Fluid Mechanics, 67(2) (1975) 349–368.
- [40] E.J. Hopfinger, J.-A. Toly, Spatially-decaying turbulence and its relation to mixing across density interfaces, Journal of Fluid Mechanics, 78 (1976) 155–175.
- [41] C.A. Schneider, W.S. Rasband, K.W. Eliceiri, NIH Image to ImageJ: 25 years of image analysis, Nature Methods, 9(7) (2012) 671–675.
- [42] P. Jarvis, B. Jefferson, J. Gregory, S.A. Parsons, A review of floc strength and breakage, Water Research, 39(14) (2005) 3121–3137.
- [43] T.R. Camp, P.C. Stein, Velocity gradients and internal work in fluid motion, Journal of the Boston Society of Civil Engineers (1943) 219–237.
- [44] B.G. Krishnappan, J. Marsalek, Modelling of flocculation and transport of cohesive sediment from an on-stream stormwater detention pond, Water Research, 36(15) (2002) 3849–3859.
- [45] F. Maggi, F. Mietta, J.C. Winterwerp, Effect of variable fractal dimension on the floc size distribution of suspended cohesive sediment, Journal of Hydrology, 343(1-2) (2007) 43–55.

- [46] B.J. Lee, E. Toorman, F.J. Molz, J. Wang, A two-class population balance equation yielding bimodal flocculation of marine or estuarine sediments, *Water Research*, 45(5) (2011) 2131–2145.
- [47] W.H. McAnally, A.J. Mehta, Significance of aggregation of fine sediment particles in their deposition, *Estuarine, Coastal and Shelf Science*, 54 (2002) 643–653.
- [48] J.C. Winterwerp, W.G.M. van Kesteren, Introduction to the physics of cohesive sediments in the marine environment. *Developments in Sedimentology*, Vol. 56. Elsevier, Amsterdam, NL, 2004.
- [49] N.-S. Cheng, Simplified settling velocity formula for sediment particle, *Journal of Hydraulic Engineering*, 123(2) (1997) 149–152.
- [50] N.-S. Cheng, Effect of concentration on settling velocity of sediment particles, *Journal of Hydraulic Engineering*, 123(8) (1997) 728–731.
- [51] M. von Smoluchowski, Versuch einer Mathematischen Theorie der Koagulations-kinetik Kolloid Lösungen, *Zeitschrift für Physikalische Chemie*, 92 (1917) 129–168, (Leipzig, in German).
- [52] C. Selomulya, G. Bushell, R. Amal, R., T.D. White, Understanding the role of restructuring in flocculation: the application of a population balance model, *Chemical Engineering Science*, 58 (2003) 327–338.
- [53] K.A. Kusters, The Influence of Turbulence on Aggregation of Small Particles in Agitated Vessels. Ph.D. thesis, Technische Universiteit Eindhoven, 1991.

Figure Captions

Fig. 1: (a) Schematic representation of settling column arrangement, oscillating grid array and in-situ floc measurement section; (b) image showing settling column during operation.

Fig. 2: (a) Inverted image of kaolin flocs settling in viewing chamber; (b) and (c) show enlarged images of individual flocs.

Fig. 3: Time series plots of OBS turbidity measurements (NTU) within grid-stirred column at mid-height (OBS_1) and bottom (OBS_2) of oscillating grid array for kaolin clay runs (a) TN3, (c) TN5, (e) TN8, and sand-clay runs (b) TNS3, (d) TNS1, (f) TNS2 (see Table 1). $OBS_1(ave)$ and $OBS_2(ave)$ are 11 min (61 point) moving-average trendlines from the raw OBS_1 and OBS_2 datasets.

Fig. 4: Temporal variations in measured floc size distributions for kaolin clay suspensions: (a) run TN1; (b) run TN3; (c) run TN4; (d) run TN5; (e) run TN7; and (f) run TN8 (see Table 1).

Fig. 5: Time series development of maximal $D_{f,95}$, $D_{f,90}$ and root-mean-square $D_{f,rms}$ floc sizes for kaolin clay suspension runs: (a) TN1, (b) TN3, (c) TN4, (d) TN5, (e) TN7, and (f) TN8 (see Table 1). Error bars on maximal $D_{f,95}$ floc sizes

represent the standard deviations in the statistically-determined values. Variations in total suspended sediment (TSS) concentration at OBS₁ and OBS₂ positions are shown for comparison.

Fig. 6: Time series development of maximal $D_{f,95}$, $D_{f,90}$ and root-mean-square $D_{f,rms}$ floc sizes for sand-clay suspension runs: (a) TNS3, (b) TNS4, (c) TNS1, (d) TNS5, (e) TNS2, and (f) TNS6 (see Table 1). Error bars on maximal $D_{f,95}$ floc sizes represent the standard deviations in the statistically-determined values. Variations in total suspended sediment (TSS) concentration at OBS₁ and OBS₂ positions are shown for comparison.

Fig. 7: Variation in peak or quasi-equilibrium representative floc sizes (a) $D_{f,95}$, (b) $D_{f,90}$, and (c) $D_{f,rms}$ versus flocculation parameter $(C_b/G)^{1/2}$ in all kaolin clay and sand-clay mixture runs. Error bars on each data point indicate ± 1 standard deviation in floc sizes (vertical) and concentrations (horizontal)..

Fig. 8: Discretisation of the main settling column section for 1DV PBE model

Fig. 9: Time series plots showing experimental measurements and 1DV PBE model predictions: (a1)-(d1) mass concentration variations at OBS₁ (i.e. cell $k = 15$) and OBS₂ (i.e. cell $k = 30$) positions; (a2)-(d2) $D_{f,95}$ and $D_{f,rms}$ floc sizes (at cell $k = 30$) for kaolin clay runs (a) TN4; (b) TN5; (c) TN7; and (d) TN8.

Fig. 10: Time series plots showing experimental measurements and 1DV PBE model predictions of $D_{f,95}$ and $D_{f,rms}$ floc sizes (at cell $k = 30$) for clay-sand runs (a) TNS2; (b) TNS5; and (c) TNS6.

Fig. 11: Time series plots of 1DV PBE model predictions of $D_{f,95}$ and $D_{f,rms}$ showing the influence of different floc break-up parameters: (a) runs TN5 and TNS5; (b) runs TN8, TNS2 and TNS6 (see Tables 1 and 2); and (c) the influence of initial floc size $D_{f,k=1}$ specification at the upper boundary of the 1DV model domain (run TN4, Table 1 and 2).

Table Captions:

Table 1: Summary of the main experimental variables

Table 2: Summary of main model parameters used in 1DV advection-diffusion PBE simulations

Table 3: Summary of measured and 1DV PBE predicted peak or quasi-equilibrium $D_{f,95}$ and $D_{f,rms}$ floc sizes for kaolin clay and sand-clay mixture runs shown.

Fig. 1: (a) Schematic representation of settling column arrangement, oscillating grid array and in-situ floc measurement section; (b) image showing settling column during operation.

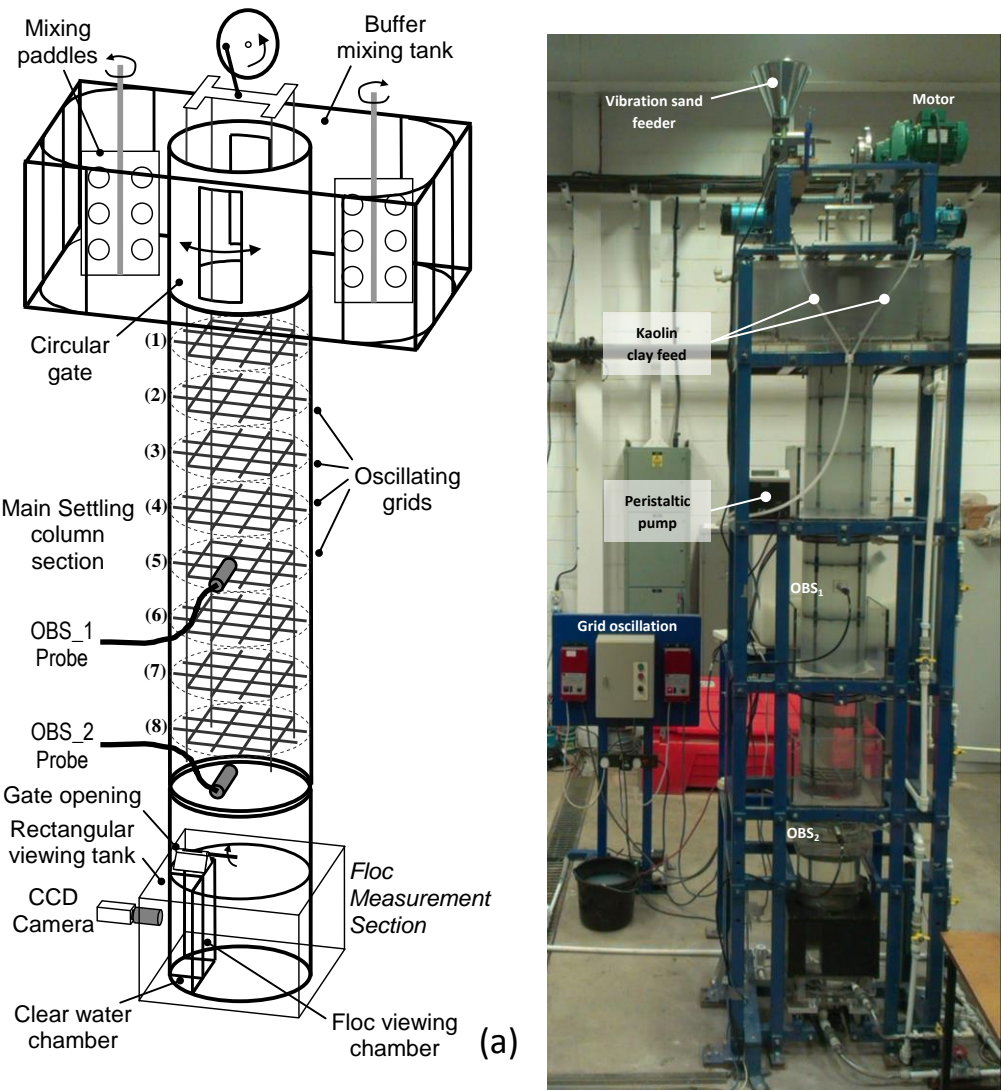


Fig. 2: (a) Inverted image of kaolin flocs settling in viewing chamber; (b) and (c) show enlarged images of individual flocs.

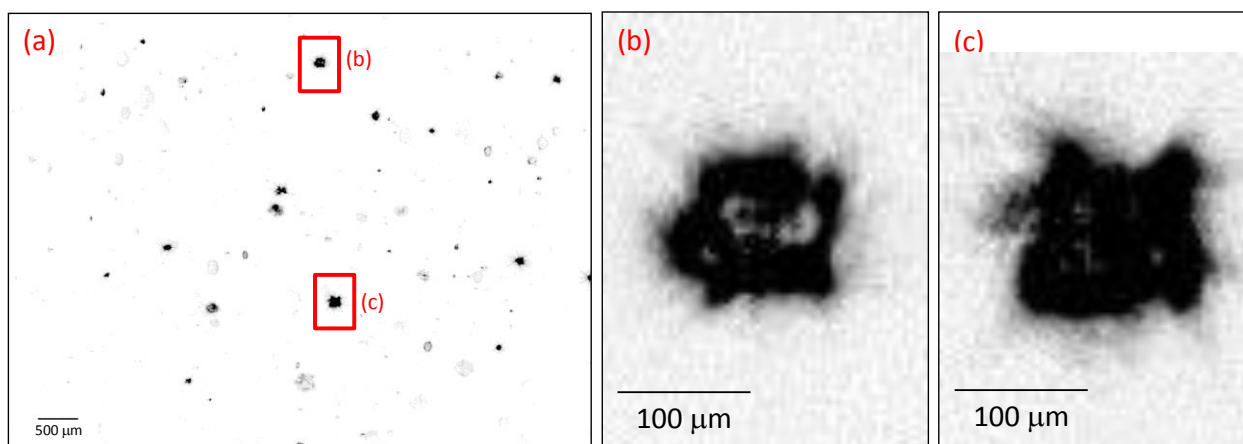


Fig. 3: Time series plots of OBS turbidity measurements (NTU) within grid-stirred column at mid-height (OBS₁) and bottom (OBS₂) of oscillating grid array for kaolin clay runs (a) TN3, (c) TN5, (e) TN8, and sand-clay runs (b) TNS3, (d) TNS1, (f) TNS2 (see Table 1). OBS₁(ave) and OBS₂(ave) are 11 min (61 point) moving-average trendlines from the raw OBS₁ and OBS₂ datasets.

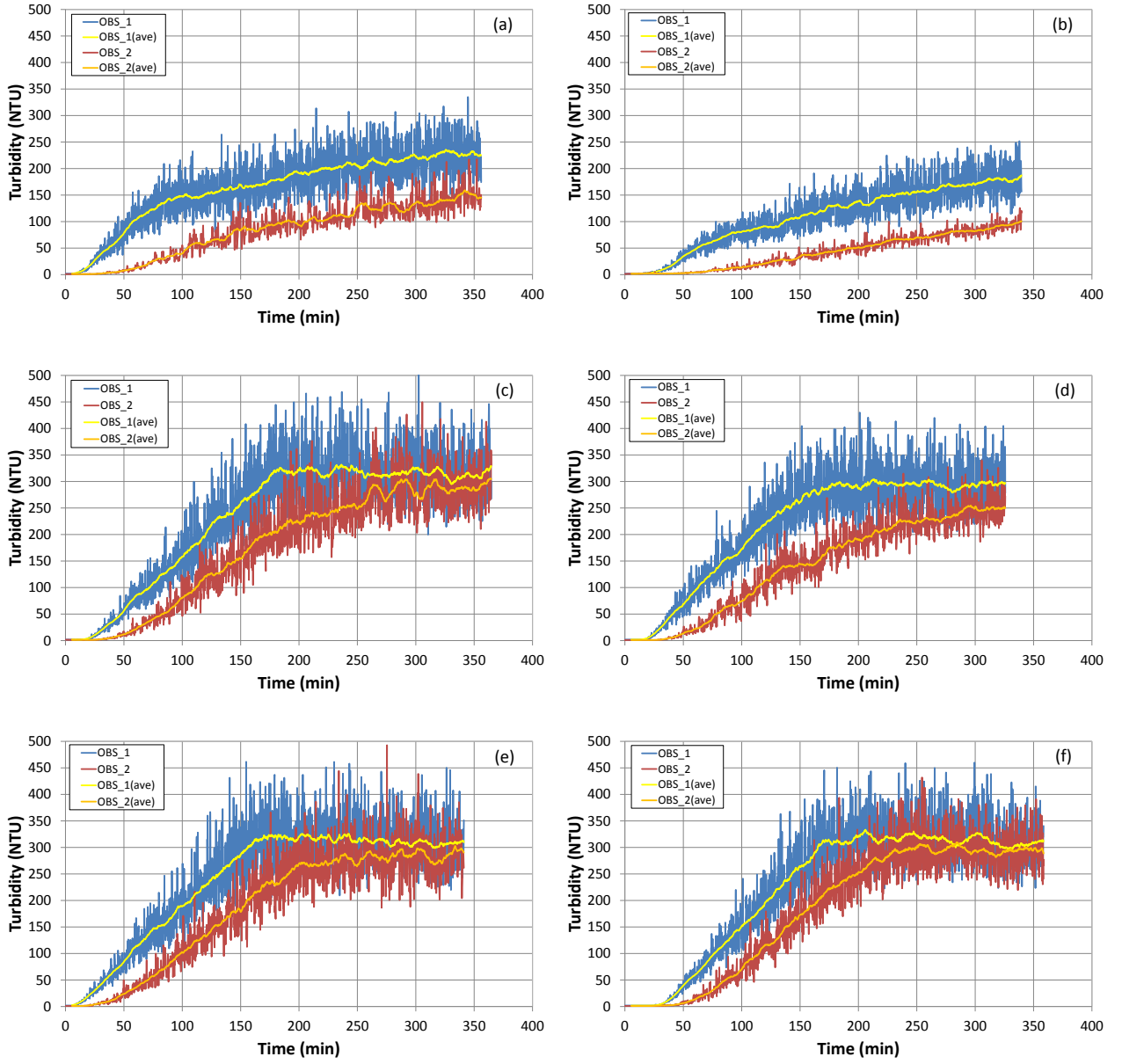


Fig. 4: Temporal variations in measured floc size distributions for kaolin clay suspensions: (a) run TN1; (b) run TN3; (c) run TN4; (d) run TN5; (e) run TN7; and (f) run TN8 (see Table 1).

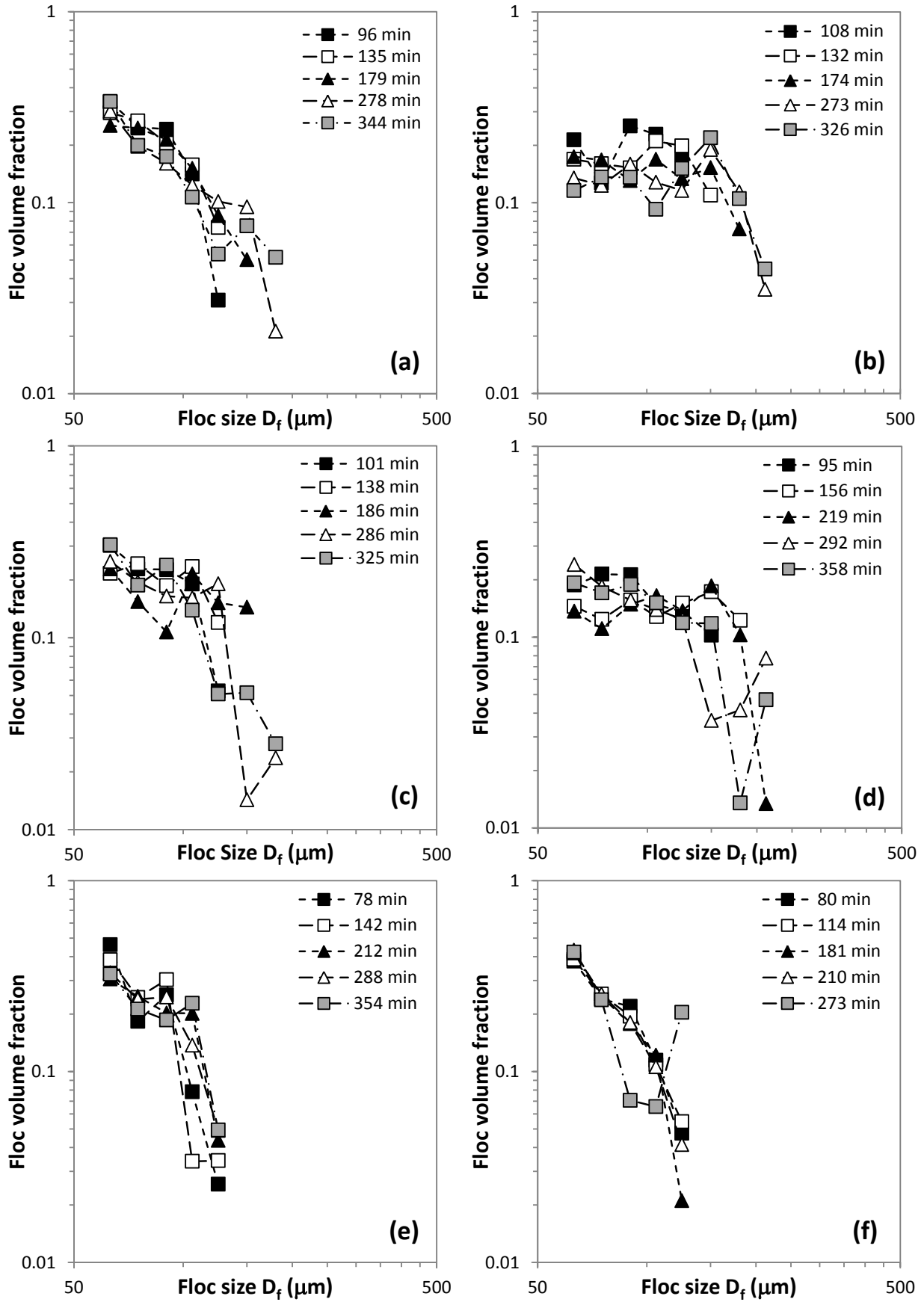


Fig. 5: Time series development of maximal $D_{f,95}$, $D_{f,90}$ and root-mean-square $D_{f,rms}$ floc sizes for kaolin clay suspension runs: (a) TN1, (b) TN3, (c) TN4, (d) TN5, (e) TN7, and (f) TN8 (see Table 1). Error bars on maximal $D_{f,95}$ floc sizes represent the standard deviations in the statistically-determined values. Variations in total suspended sediment (TSS) concentration at OBS₁ and OBS₂ positions are shown for comparison.

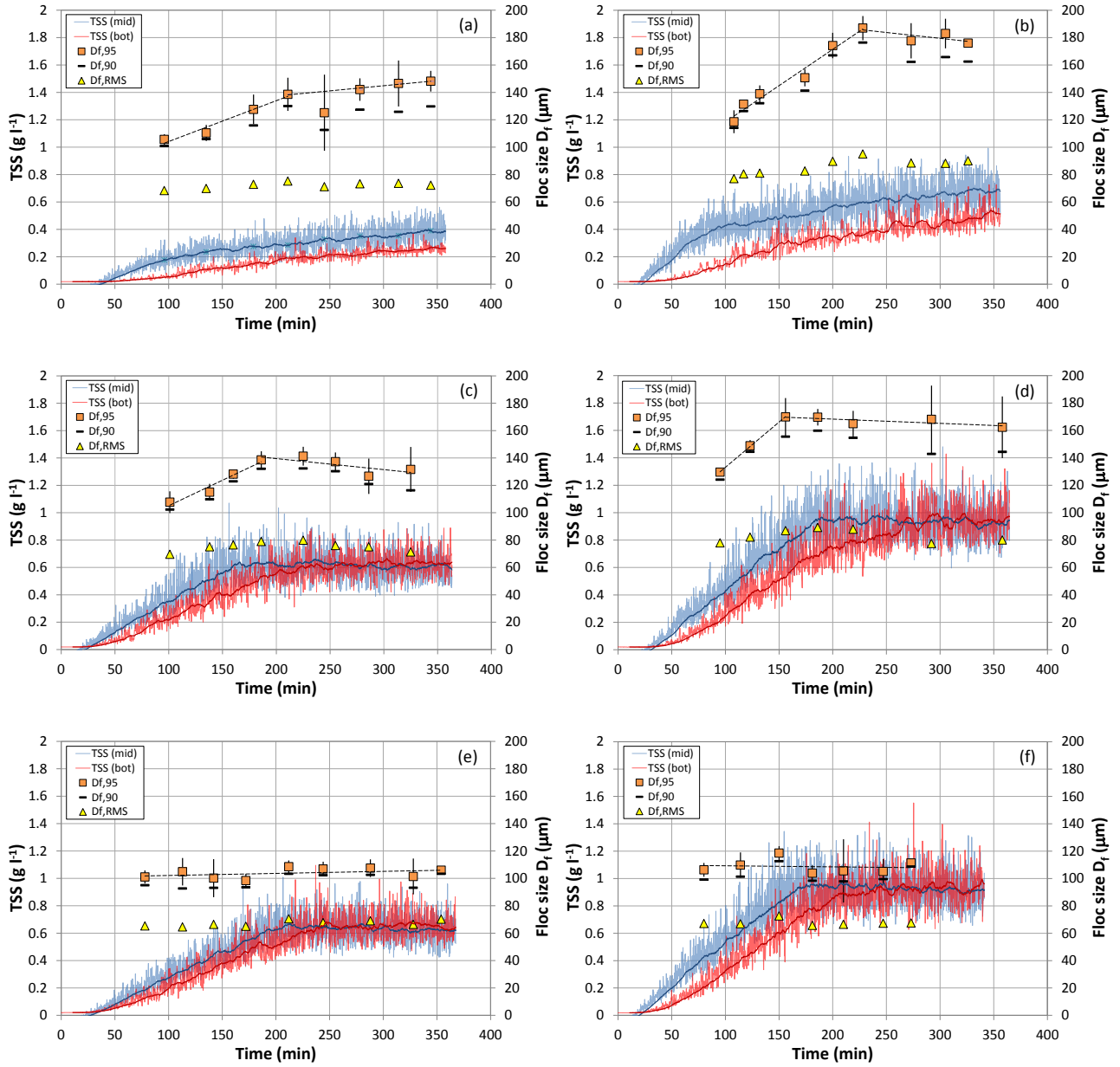


Fig. 6: Time series development of maximal $D_{f,95}$, $D_{f,90}$ and root-mean-square $D_{f,rms}$ flocc sizes for sand-clay suspension runs: (a) TNS3, (b) TNS4, (c) TNS1, (d) TNS5, (e) TNS2, and (f) TNS6 (see Table 1). Error bars on maximal $D_{f,95}$ flocc sizes represent the standard deviations in the statistically-determined values. Variations in total suspended sediment (TSS) concentration at OBS₁ and OBS₂ positions are shown for comparison.

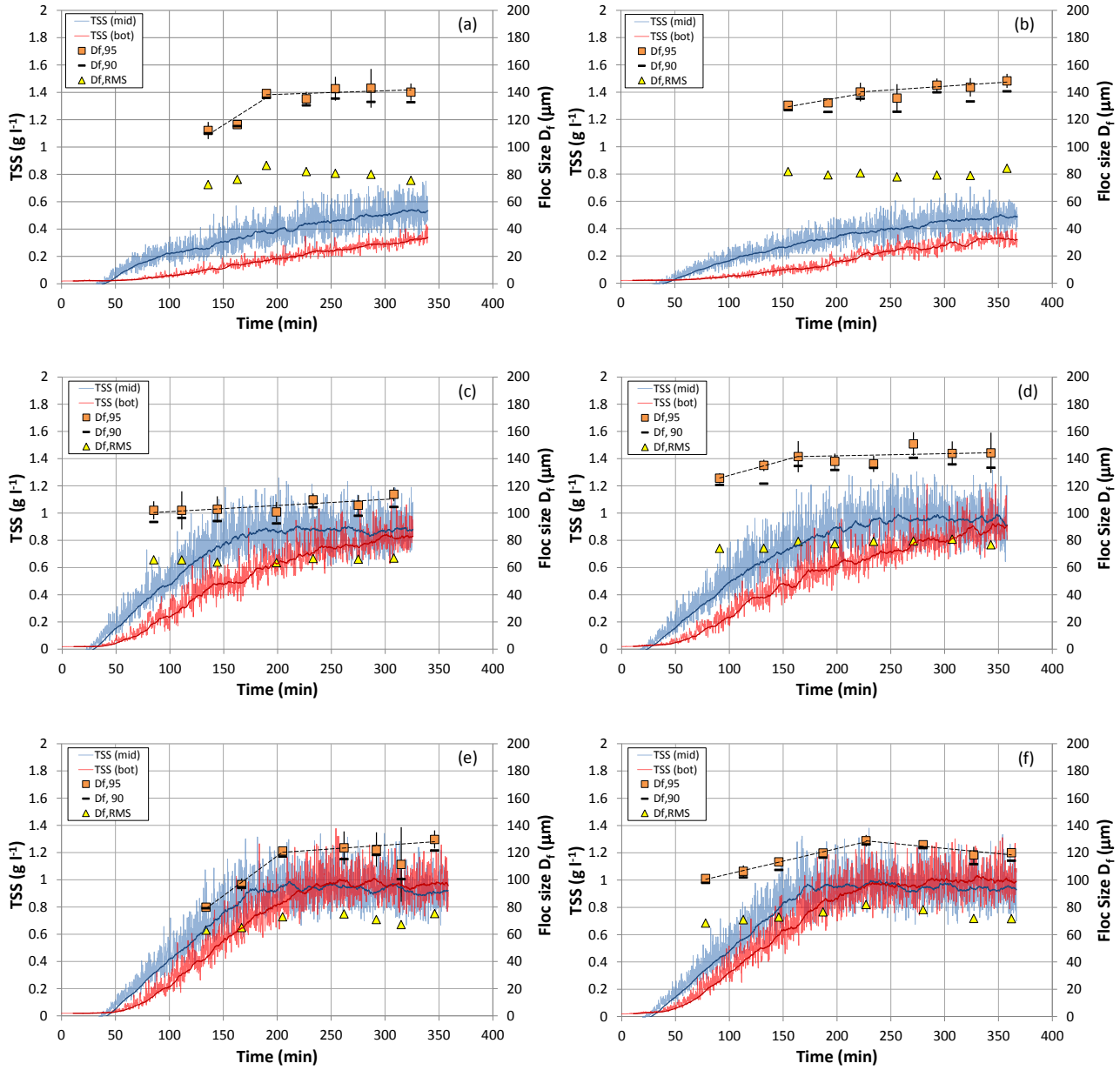


Fig. 7: Variation in peak or quasi-equilibrium representative flocculation parameters (a) $D_{f,95}$, (b) $D_{f,90}$, and (c) $D_{f,rms}$ versus flocculation parameter $(C_b/G)^{1/2}$ in all kaolin clay and sand-clay mixture runs. Error bars on each data point indicate ± 1 standard deviation in flocculation parameters (vertical) and concentrations (horizontal).

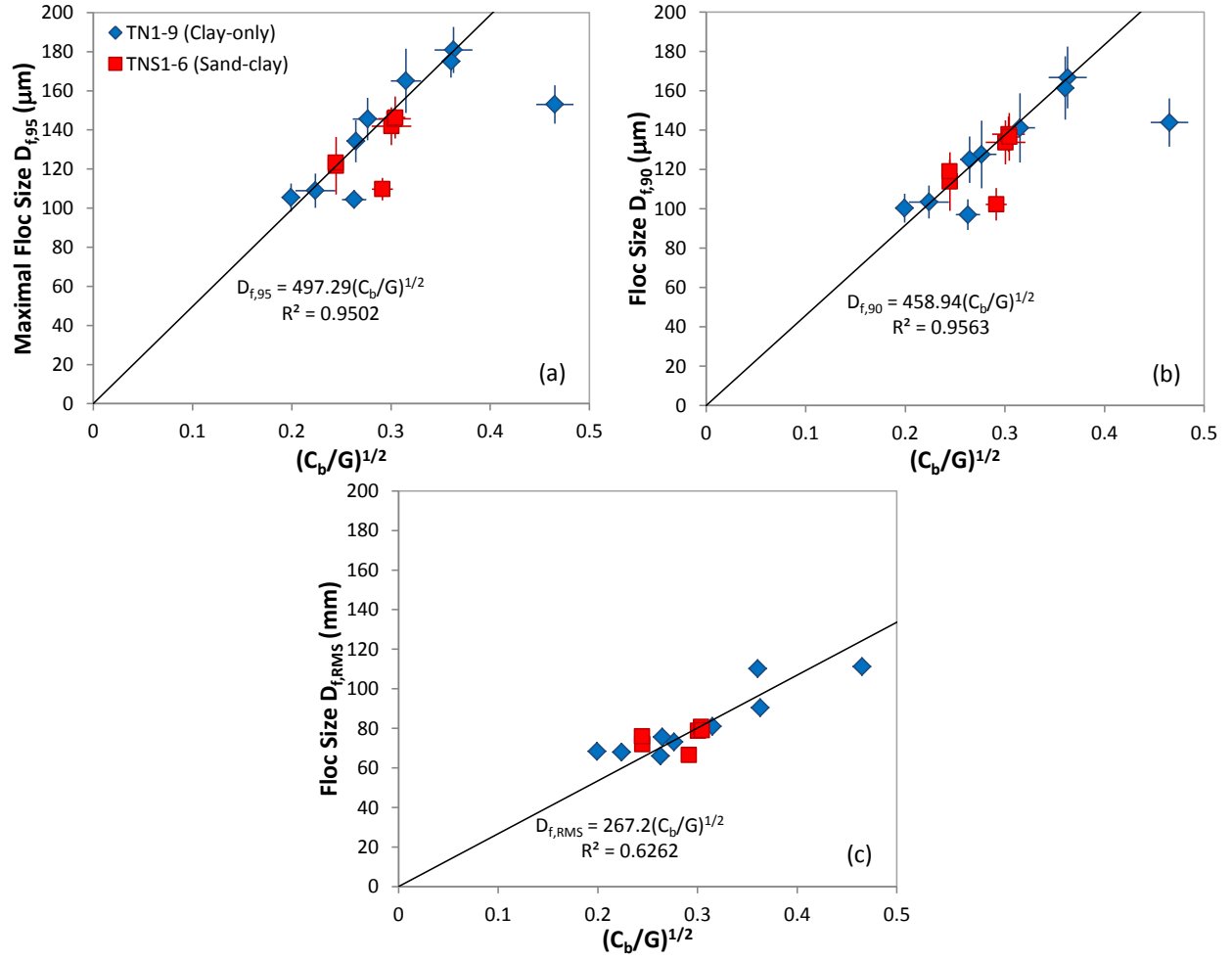


Fig. 8: Discretisation of the main settling column section for 1DV PBE model

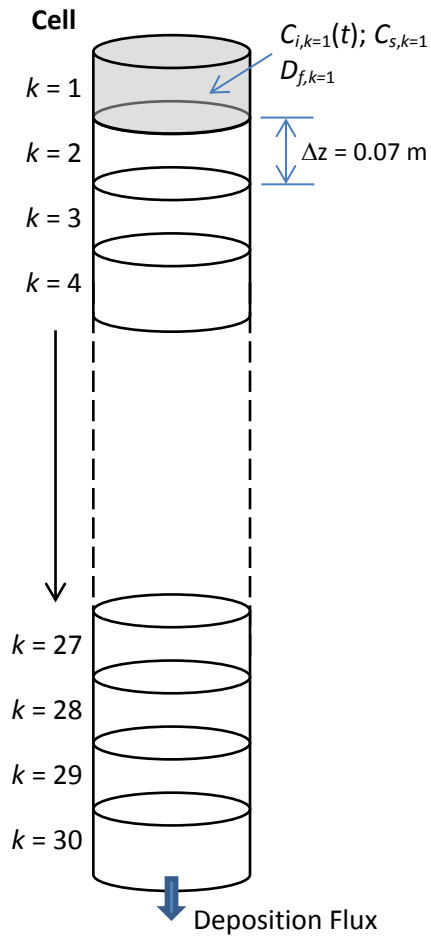


Fig. 9: Time series plots showing experimental measurements and 1DV PBE model predictions: (a1)-(d1) mass concentration variations at OBS₁ (i.e. cell $k = 15$) and OBS₂ (i.e. cell $k = 30$) positions; (a2)-(d2) $D_{f,95}$ and $D_{f,rms}$ floc sizes (at cell $k = 30$) for kaolin clay runs (a) TN4; (b) TN5; (c) TN7; and (d) TN8.

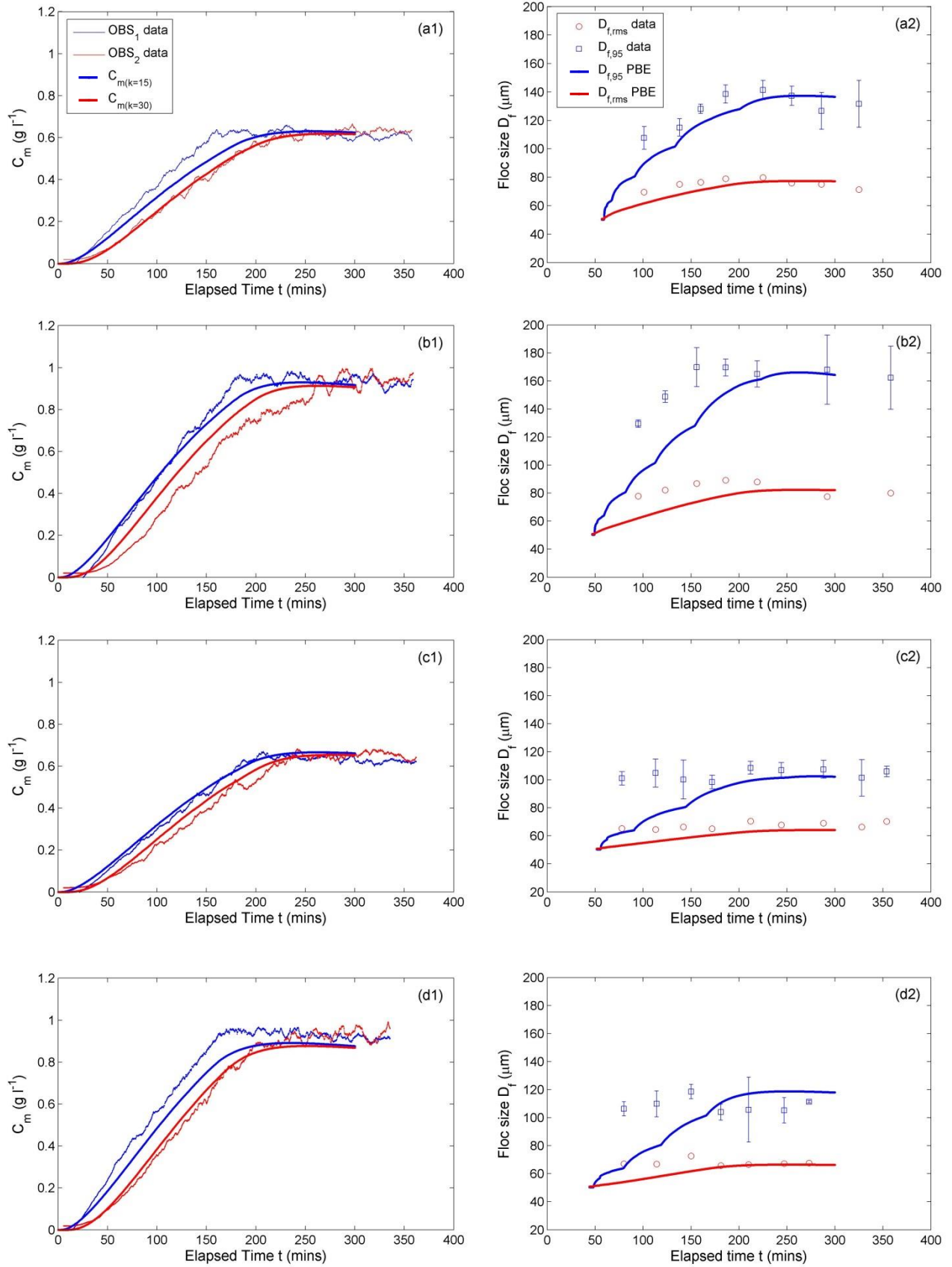


Fig. 10: Time series plots showing experimental measurements and 1DV PBE model predictions of $D_{f,95}$ and $D_{f,rms}$ flocc sizes (at cell $k = 30$) for clay-sand runs (a) TNS2; (b) TNS5; and (c) TNS6.

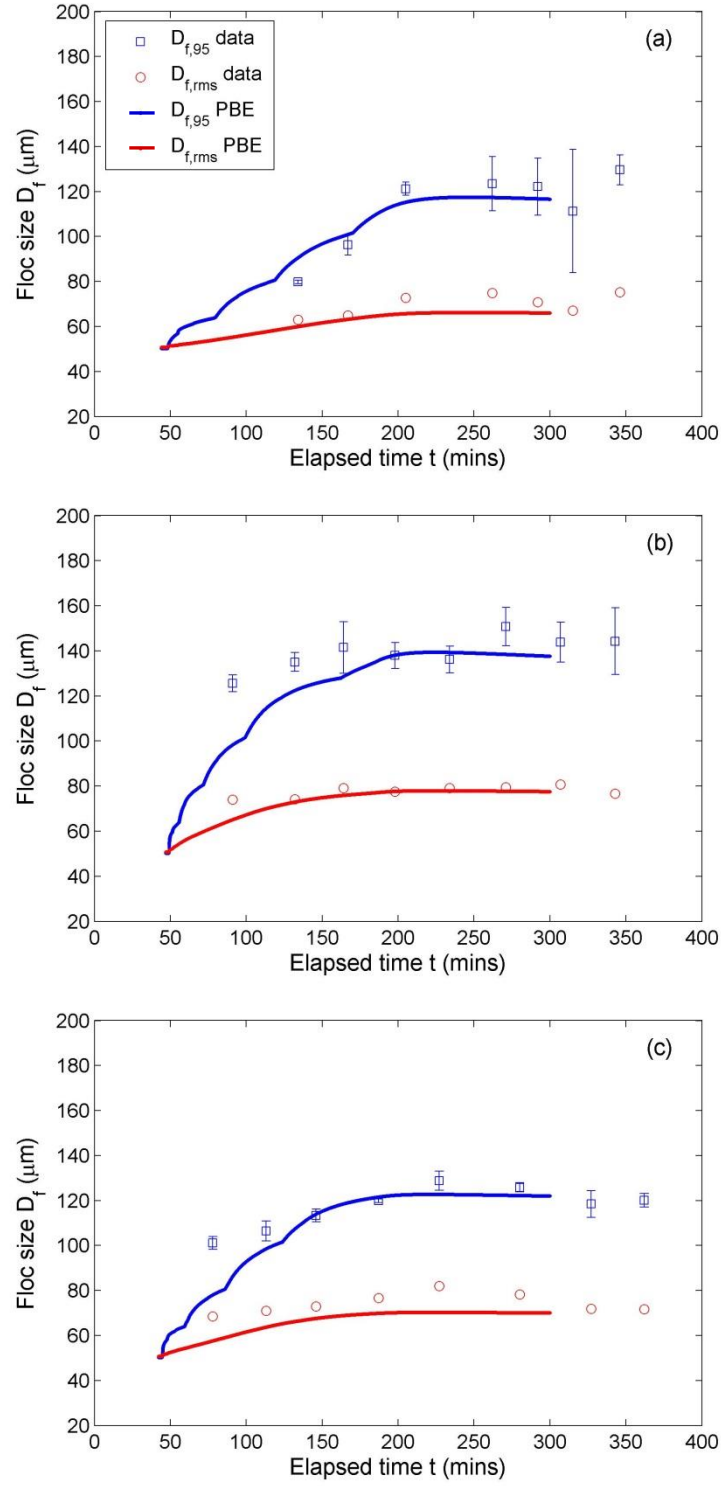


Fig. 11: Time series plots of 1DV PBE model predictions of $D_{f,95}$ and $D_{f,rms}$ showing the influence of different floc break-up parameters: (a) runs TN5 and TNS5; (b) runs TN8, TNS2 and TNS6 (see Tables 1 and 2); and (c) the influence of initial floc size $D_{f,k=1}$ specification at the upper boundary of the 1DV model domain (run TN4, Table 1 and 2).

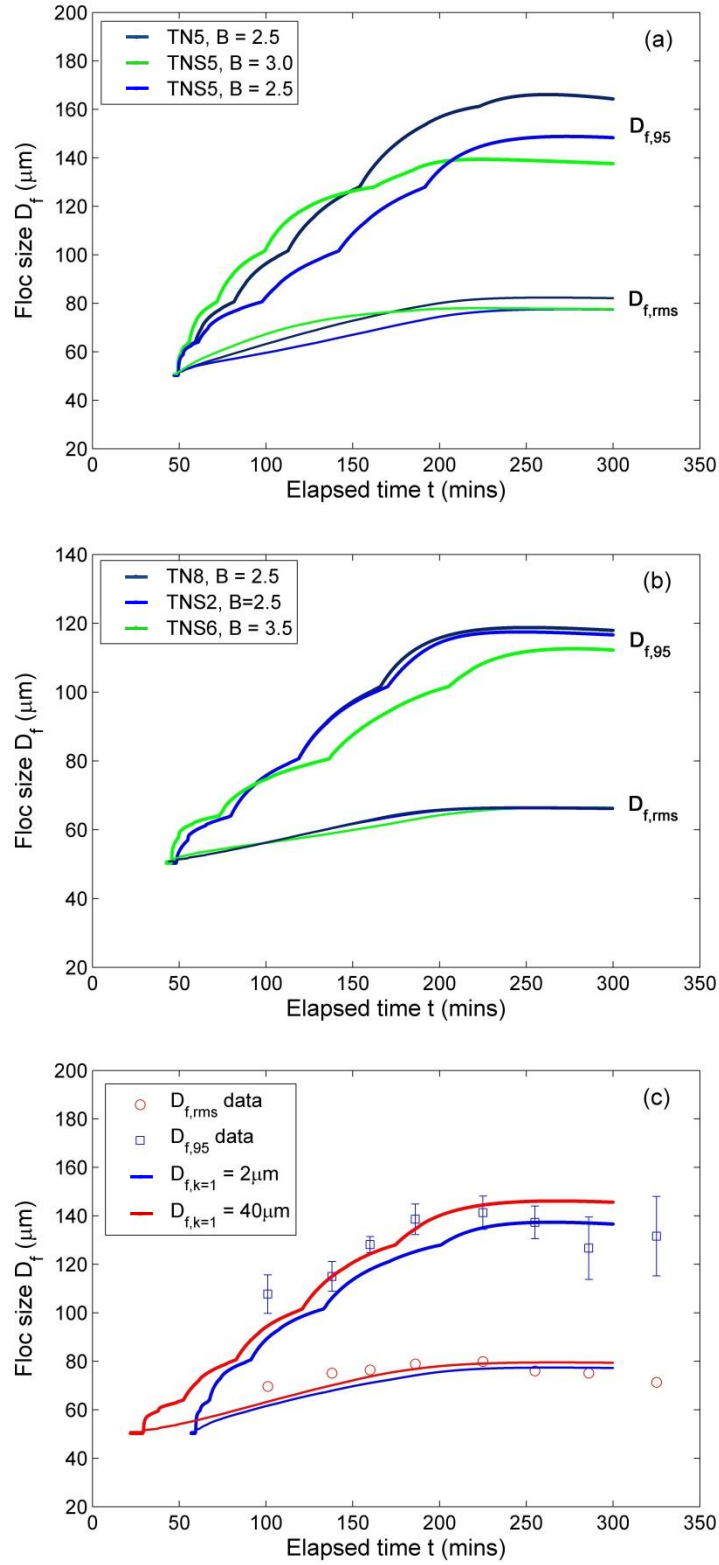


Table 1: Summary of the main experimental variables

Run No.	Oscillating Grids				Kaolin-water mixture			Dry sand
	Stroke S (m)	Frequency f (s^{-1})	Shear rate G_{min} (s^{-1}) [*]	Shear rate G_{max} (s^{-1}) [*]	Concentration C_m (g l^{-1})	Feed rate Q_m (l min^{-1})	Feed time t_m (mins)	Feed rate I_s (g min^{-1})
TN1	0.05	0.2	0.73	43.6	1.2	0.3	190	-
TN2	0.05	0.2	0.73	43.6	2.4	0.3	190	-
TN3	0.05	0.2	0.73	43.6	1.8	0.3	169	-
TN4 ⁺	0.05	0.4	2.07	123.5	1.2	0.3	152	-
TN5 ⁺	0.05	0.4	2.07	123.5	1.8	0.3	170	-
TN6	0.05	0.4	2.07	123.5	2.4	0.3	163	-
TN7 ⁺	0.05	0.6	3.79	226.8	1.2	0.3	192	-
TN8 ⁺	0.05	0.6	3.79	226.8	1.8	0.3	155	-
TN9	0.05	0.6	3.79	226.8	2.4	0.3	215	-
TNS1	0.05	0.4	2.07	123.5	1.8	0.3	172	2.26
TNS2 ⁺	0.05	0.6	3.79	226.8	1.8	0.3	157	1.99
TNS3	0.05	0.2	0.73	43.6	1.8	0.3	140	2.0
TNS4	0.05	0.2	0.73	43.6	1.8	0.3	150	4.15
TNS5 ⁺	0.05	0.4	2.07	123.5	1.8	0.3	170	3.90
TNS6 ⁺	0.05	0.6	3.79	226.8	1.8	0.3	180	4.70

^{*} Test runs for PBE model simulations
^{*} Based on predictions from Eq. (2) at the mid-elevation between grids (i.e. $z/H = 0$) and close to “rest” position of grids (i.e. $z/H = \pm 0.475$)

Table 2: Summary of main model parameters used in 1DV advection-diffusion PBE simulations

Run No.	Shear rate G (s^{-1})	Clay diffusion $\Gamma_{s,i}$ ($m^2.s^{-1}$)	Sand diffusion Γ_s ($m^2.s^{-1}$)	Floc break-up parameter B^+	Floc collision efficiency α_{max}	Initial floc diameter $D_{f(k=1)}$ (μm)	Sand input concentration $C_{s(k=1)}$ ($g.l^{-1}$)	Sand-floc collision efficiency $\alpha_{i,M+1}$
TN4	75.0	50×10^{-5}	0.5×10^{-5}	3.0	1.0	2.0	-	-
TN5	75.0	50×10^{-5}	0.5×10^{-5}	2.5	1.0	2.0	-	-
TN7	100.0	50×10^{-5}	0.5×10^{-5}	3.0	1.0	2.0	-	-
TN8	100.0	50×10^{-5}	0.5×10^{-5}	2.5	1.0	2.0	-	-
TNS2	100.0	50×10^{-5}	0.5×10^{-5}	2.5	1.0	2.0	0.0105	0.5 (150) [*]
TNS5	75.0	50×10^{-5}	0.5×10^{-5}	3.0	1.0	2.0	0.0205	0.5 (150) [*]
TNS6	100.0	50×10^{-5}	0.5×10^{-5}	4.0	1.0	2.0	0.0247	0.5 (150) [*]

⁺ Used to calculate critical energy dissipation term ε_{bi} causing floc break-up [Eq. (22)]

^{*} Minimum floc size for sand-floc interaction and break-up [$D_i \geq D_{si}$, Eq. (24)]

Other fixed coefficients and empirical constants used in 1DV PBE model parameters:

Eq. (16): maximum floc-floc collision efficiency $\alpha_{max} = 1.0$; fitting parameters $x = y = 0.1$

Eq. (17): Boltzmann constant $K_B = 1.38 \times 10^{-23} m^2.kg.s^{-2}.K^{-1}$; absolute temperature $T = 293K$ (20°C)

Table 3: Summary of measured and 1DV PBE predicted peak or quasi-equilibrium $D_{f,95}$ and $D_{f,rms}$ floc sizes for kaolin clay and sand-clay mixture runs shown.

Run No.	Settling Column		1DV PBE Model		Percentage Differences (%)	
	$D_{f,95(1)}$ (μm)	$D_{f,rms(1)}$ (μm)	$D_{f,95(2)}$ (μm)	$D_{f,rms(2)}$ (μm)	$[D_{f,95(2)} - D_{f,95(1)}] / D_{f,95(1)} \times 100$	$[D_{f,rms(2)} - D_{f,rms(1)}] / D_{f,rms(1)} \times 100$
TN4	134.2	75.6	137.4	77.4	2.38	2.38
TN5	165.1	81.0	166.1	82.4	0.61	1.73
TN7	105.4	68.3	102.5	64.2	-2.75	6.00
TN8	108.9	68.0	118.8	66.5	9.09	-2.21
TNS2	121.6	72.0	117.5	66.2	-3.37	-8.06
TNS5	146.3	79.0	139.5	78.0	-4.65	-1.27
TNS6	123.3	76.0	122.8	70.3	-0.41	-7.50